Bachelor Thesis

Influence of dopants in the creation yield of NV centers

March 31, 2020

Universität Leipzig

Faculty of Physics and Earth Sciences

Felix Bloch Institute for Solid State Physics

Applied Quantum Systems (AQS)

Submitted by:
Efrain Insuasti Pazmiño
3736902

Examiners:
Prof. Dr. rer. nat. Habil. Jan Meijer
Dr. rer. nat. Ralf Wunderlich

Page intentionally left blank.

Contents

List of Figures

List of Tables

Chapter 1

Introduction

Diamonds have fascinated human-beings for over 5000 years [1]. In the 16th century, black and indigenous slaves were forced to mine them in the Brazilian colonies [2]. Four centuries later, the successes in quantum technologies and the development of methods to produce high purity artificial diamonds created a boost in the research of diamond. Nowadays, diamond research based applications can revolutionize the world.

Suitable hosts for quantum information technologies can be realized using defect-related optical centres in diamond. It is therefore, due to the large number of optically active defects, a promising platform for exploring properties at the quantum scale [3]. Nevertheless, creating a quantum computer based on NV centers as suitable q-bits, technological difficulties must be still overcome. In fact, up to now a deterministic generation of NV centers is still not possible [4].

In order to build a scaleable quantum technology, two conflicting demands need to be addressed: A well isolated system -such as a single trapped atom that can be controlled with high precision- as well as scale-able technology [5]. In other words, it becomes necessary to control, at the highest level, the number and positioning of dopant atoms which are introduced in the devices by ion implantation [6]. Recent work has been focused on controlling the NV charge state, whose stability strongly depends on its electrostatic environment[7]. In this thesis, such an environment is modified by the addition of different dopants (acceptors and donors) into the diamond lattice through ion beam implantation.

Chapter two of this study is devoted to the build up of the framework of the physics of diamond, emphasizing its crystalline and electronic structure and properties. Additionally, the definition and description of the NV centres is discussed. NV centres can have two stable charge states with photo-induced interconversion between them [8]. Finally, the interaction of ion beams with matter is described in terms of the energy losses and limiting factors of the spatial resolution. Channeling leads to a loss of the resolution in the depth direction and ion struggling associates to an uncertainty in the final position of each single implanted ion [6].

Chapter three concerns the description of the methods used for preparing the sample for measurement. A 100kV particle accelerator is used to implant the selected dopants and damaging ions into the sample. A high temperature oven is used for the annealing steps, and a plasma chamber is used to clean the undesired graphitization on the surface of the diamond. The measurement itself is carried out by means of a confocal microscope -that allows the measurement of the fluorescence of the created color centers- and a grating spectrometer that gives the wavelength resolved fluorescence.

The sequence of steps carried out in the experiment is presented in chapter four. Its design as well as the actual mathematical simulations are presented here. Special attention has been put on the description and conditions used for every measurement and the methodological division of the sample in order to facilitate its further analytical discussion.

In chapter five the results of the experiments are presented and a discussion about the main findings is shown. Neutrally charged vacancies in boron and sulphur doped diamond are measured before an irreversible diffusion of the vacancies through an annealing step. Next, NV^0 and NV^- centres are discussed for both S and B-doped diamond as well as the regions outside them. Additionally an attempt is done to determine the yield of NV centres. Finally, the last chapter presents the summary and conclusions of this study.

Chapter 2

Theory

2.1 Physics of diamond

Diamond is a natural allotrope of carbon in which the atoms are arranged in a crystal diamond cubic structure. Diamond is transparent and insulating, a good thermal conductor at room temperature and the hardest naturally occurring material on earth [9].

2.1.1 Crystal Structure

The diamond structure belongs to the crystal class T_d. It allows three dimensional covalent bonding in which every atom is surrounded by four nearest neighbors in a tetrahedral configuration [10]. The diamond structure can be described as two interpenetrating fcc structures, displaced relative to one another along the main diagonal as seen in figure 2.1.

The diamond structure is relatively empty: the maximum proportion of the available volume which may be filled by hard spheres is only 0.34, which is 46 percent of the filling factor for a closest-packed structure. Its lattice constant is $a = 3.567\,\text{Å}$ [11].

Diamond is typical of the crystal structures formed by elements from column IV of the period table: carbon, silicon, germanium and tin. These elements all crystallize in the tetrahedrally coordinated diamond structure [12].

2.1.2 Electronic Structure

The band structure of a solid is the range of electron energies that the solid may have within it (also called energy bands or allowed bands) or may not have (called forbidden bands or band gaps). The electrons of a single atom occupy atomic orbitals with a discrete energy level. When two or more atoms join together to form into a molecule, their atomic orbitals overlap[12].
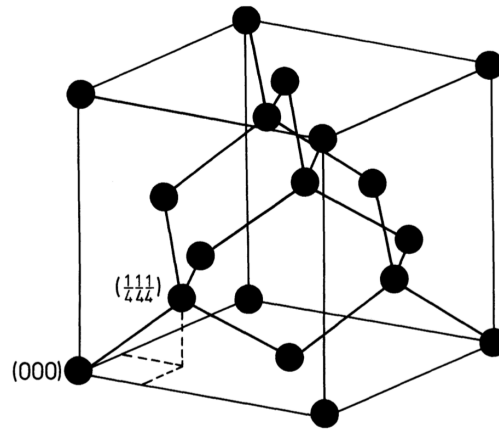
Figure 2.1: Diamond crystal structure consisting of two interpenetrating fcc structures, taken from [10].

The band structure of a solid lets us understand its optical and electrical properties. To calculate it one can start with the time independent Schrödinger equation for a single electron [10].

$$\left[-\frac{\hbar}{2m}\nabla^2 + U(\mathbf{r})\right]\Psi(\mathbf{r},\mathbf{k}) = E(\mathbf{k})\hat{H}\Psi(\mathbf{r},\mathbf{k}) \tag{2.1}$$

The potential $U(\mathbf{r})$ is periodic so it fulfills $U(\mathbf{r}) = U(\mathbf{r}+\mathbf{R_n})$. $\mathbf{r}$ is a lattice vector and $\mathbf{R_n}$ is an arbitrary translation vector of the three dimensional periodic lattice. According to the Block's theorem, the eigenstates are:

$$\Psi(\mathbf{r},\mathbf{k}) = e^{i\mathbf{kr}}U_b(\mathbf{r},\mathbf{k}) \tag{2.2}$$

b represents the band index and $U_b(\mathbf{r},\mathbf{k})$ and $\Psi(\mathbf{r},\mathbf{k})$ are periodic in R.

$$\begin{aligned}\Psi(\mathbf{r}+\mathbf{R},\mathbf{k}) &= e^{i\mathbf{k}(\mathbf{r}+\mathbf{R})}U_b(\mathbf{r}+\mathbf{R},\mathbf{k})\\ &= e^{i\mathbf{kr}}e^{i\mathbf{kR}}U_b(\mathbf{r},\mathbf{k})\\ &= e^{i\mathbf{kR}}\Psi(\mathbf{r},\mathbf{k})\end{aligned} \tag{2.3}$$
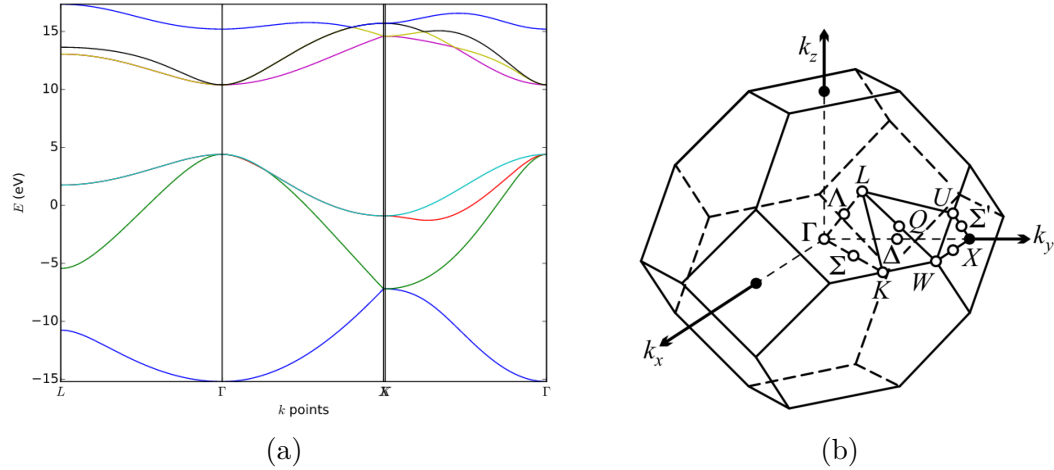
Figure 2.2: (a) Band structure of diamond for the symmetry points L to Γ [13]. The region in which no line crosses is called band gap or forbidden band(b) First Brillouin zone of the fcc cubic diamond with special points and lines. At the center the Γ point exhibits the highest symmetry [14].

A consequence of the Bloch theorem is that the energy $E(\mathbf{k}) = E(\mathbf{k} + \mathbf{G})$ is periodic in the reciprocal lattice, G denotes a lattice vector in the reciprocal space. Due to this periodicity, it is sufficient to determine the electronic structure of the entire solid body by restricting the consideration of the lattice vectors to the surroundings of a point in reciprocal space. For doing so one looks at the first Brillouin zone (BZ1) of the solid, since each wave vector can be projected into a point within the first Brillouin zone in reciprocal space. The BZ1 of the diamond structure is shown in figure 2.2b. The lines Δ, Λ and Σ join the center $\Gamma = (0, 0, 0)$ with the center $X = (2\pi/a)(0, 0, 1)$ of a square face, the center L of a hexagonal face, and an edge center K of a hexagonal face, respectively. The band structure of diamond along these directions is shown in 2.2a.

There exist several methods for calculating the band structure of diamond like tight binding, the empirical pseudo potential method (EPM) [15] or linear combination of atomic orbitals (LCAO)[16]. This methods can contradict each other [17]. The upper bands in 2.2b are called conduction bands and the lower bands are called valence bands. The separation between the lowest energy in the conduction band and the highest energy in the valence band is called the band or energy gap E_g.

2.1.3 Optical properties

The large band gap of the diamond ($E_g = 5, 45eV$) prevents the valence electrons from absorbing in the visible range of the electromagnetic spectrum of $E_{vis} \approx 1.5 - 3eV$. Note ($E_{vis} < E_g$). Therefore the diamond is transparent under visible light with a small absorption coefficient in the range of $5 \times 10^{-3} cm^{-1}$.

The inelastic scattering of the light on phonons can be observed when exposed to visible light. In Raman spectroscopy, this effect is used for structural analysis, since the crystal structure is characterized by the interatomic bonds and the associated lattice vibrations. The bonds in the solid state link the movements of the atoms to one another. The mathematical view of the atoms as a system of coupled oscillators results in characteristic vibrational frequencies ω, which are dependent on the wave vector $\vec{k}$ in the crystal structure (dispersion relation, fig. 2.2b).

Raman scattering and infrared absorption The absorption (emission) of a single phonon ($\hbar\omega$) with the creation (annihilation) of a quantum of a normal mode of vibration (phonon) in crystals requires that an oscillating dipole moment accompany the normal mode. Additionally the energy and momentum conservation of the vector $\vec{k}$ should be satisfied. Thus the resonance absorption occurs at $\hbar\omega = \hbar\omega_{\mathbf{q}}$, where $|\mathbf{q}| \sim 0$ in the infrared region [18]. Inelastic light scattering of visible monochromatic radiation (wavelength λ_L, angular frequency ω_L, wave vector in the medium $\vec{k}_L$) by a crystal fulfills again $\vec{k}$ conservation of momentum and energy. The latter means frequency shifts with respect to ω_L being $\pm\omega_{\mathbf{q}}$, $(-)$ for phonon absorption $(+)$ for emission. The wave vector of the phonon participating in the scattering process satisfies

$$|\mathbf{q}| = 2|\mathbf{k}_L| \sin(\theta/2) \tag{2.4}$$

where θ is the scattering angle. For visible light, $\mathbf{q}$ is located near the centre of the Brillouin zone ($|\mathbf{q}| \sim 0$), see fig 2.2b. Therefore Raman scattering can occur only if a single phonon is absorbed or emitted.

First order Raman line. Is is located at $1332.5\,\text{cm}^{-1}$ in an undisturbed diamond lattice. The line results from scattering on triply degenerate transverse optical (TO) phonons. The spectral position of the diamond Raman line in the Stokes (absorption) and anti-Stokes (emission) regions are different, being about 1333 and 1325 respectively [19].

Radiation B-band A broad band of width 0.5 eV at $770\,\text{nm}$ appearing in ion irradiated low-N diamonds after subsequent annealing at temperatures above 600 $^\circ C$. The band may be strong in diamonds implanted with donor impurities. The B-band is strongly quenched by N impurity ion form.

GR center. The nature of the GR center is unambiguously attributed to the neutral single vacancy V^0. The GR1 electronic transition occurs between a ^1E doubly degenerate ground orbital state and the $^1T_2(C_{3v})$ triply degenerate orbital excited state in the defect of T_d point symmetry [19].

2.1.4 Defects

Mechanical and electrical properties of solids are largely controlled by defects in the periodic structure.[10]. The most important kinds of defects are:

Vacancies These are point defects consisting of the absence of ions. They can profoundly alter the optical properties of crystals, in particular their color. Their presence is a normal thermal equilibrium phenomenon, so they can be an intrinsic feature of real crystals[12].

Interstitials It is often not the case that when a vacancy is generated the atom moves to the surface of the crystal. It may also occupy a position that is not occupied in a perfect crystal. If considering atoms in a crystalline structure as spheres there may be large enough regions among them for a new atom to fit in (especially when neighboring atoms are slightly displaced). The narrow space among the original atoms is an interstice, so an atom occupying it is called an interstitial atom or simply an interstitial [14].

Dislocations These are line defects which are almost invariably present in any real crystal. They are responsible in explaining the strength and observed rates of crystal growth [12].

Defects in diamond. There are more than one hundred identified luminiscent defects in diamond [20]. The N defects are relevant in this work. N is a defect which either exists as a single substitutional impurity or in aggregated form. The first one has an infrared local mode of vibration at $1344\,\mathrm{cm}^{-1}$ in the infrared region. The second ones are, most commonly, pairs of neighbouring substitutional atoms, the A aggregates, and groups of four around a vacancy, the B aggregate. All three forms of nitrogen impurities have distinct infrared spectra. Due to their importance, the NV centers are treated separately in this work.

2.1.5 Classification

The classification of diamonds is based on the content of N, the most common impurity. Type I diamonds are defined as containing sufficient N to be measurable by IR absorption spectroscopy (20-3000*ppm*), whereas type II diamonds do not contain enough N to be detected using the same method ($N < 5ppm$). Type I diamonds are divided into type Ia and type Ib. Both subgroups contain nitrogen, but the N atoms in each are arranged differently (see fig. 2.3). In type Ib diamonds, single N atoms that have replaced carbons in the lattice are isolated from one another; i.e., they generally do not occur in adjacent lattice positions. On the other side type Ia diamonds contain N atoms that are in close proximity to one another in one of two spectroscopic detectable configurations. The other configuration involves four N atoms that symmetrically surround a vacancy [21][22].

Type II diamonds are divided into types IIa and IIb (fig. 2.3). Type IIa diamonds contain no easily measurable N or B impurities. Type IIb diamonds contain B impurities that are thought to be isolated single atoms that replace C in the diamond lattice.
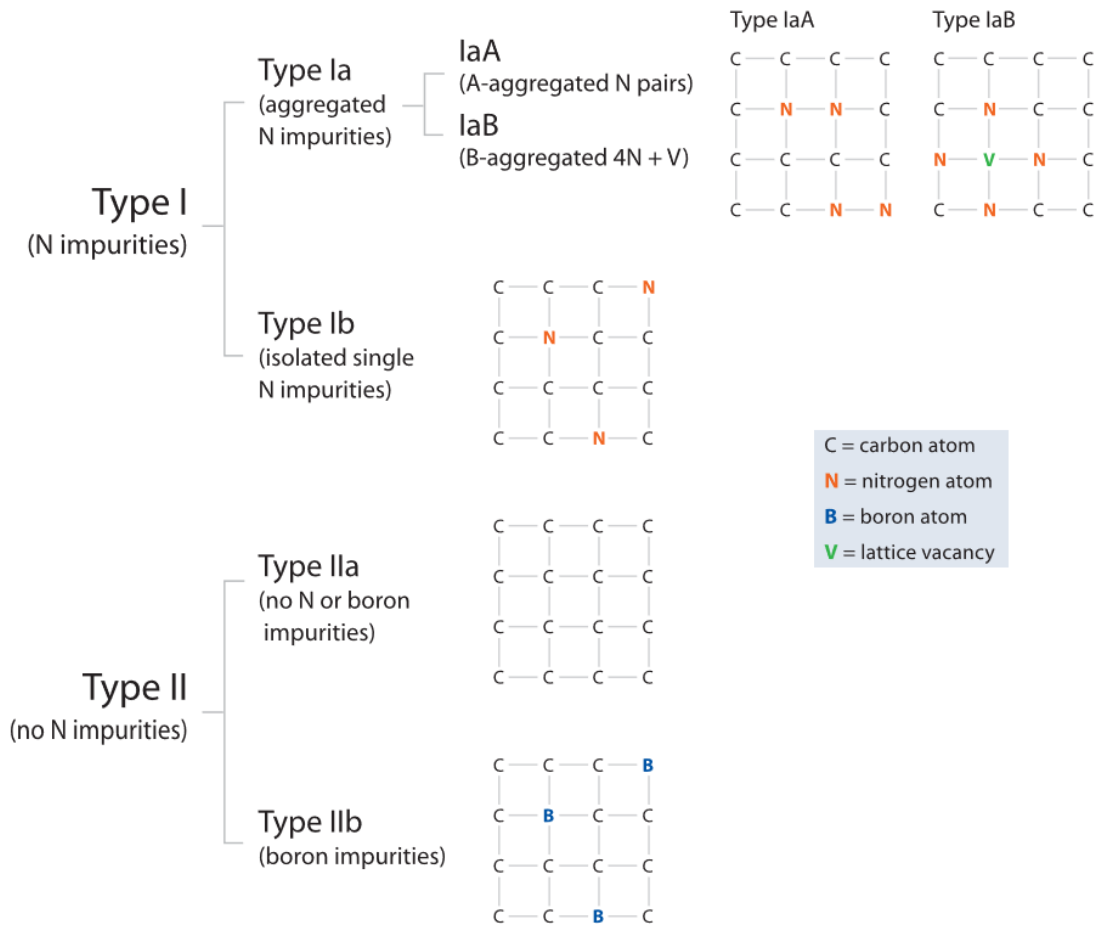
Figure 2.3: Diamond classification after [21]. The diagrams are 2D representations of the tetrahedrally bonded C atoms that form the three-dimensional diamond lattice.
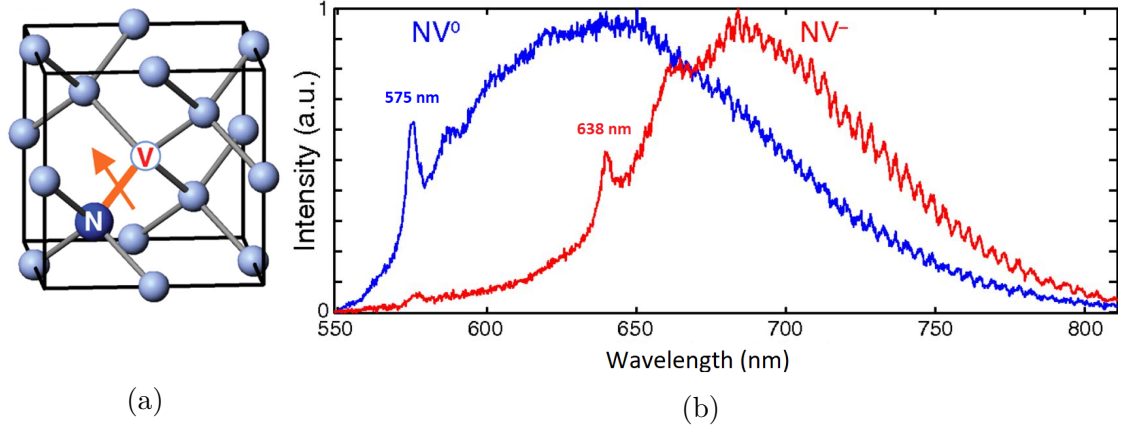
Figure 2.4: (a) Representation of a NV center in the unit cell of diamond after [25] . Spin projections $m_s = 0, \pm 1$ are defined with respect to the NV symmetry axis. (b) Characteristic spectra of NV^0 ■ and NV^- ■ with their respective ZPL peaks, after [7]

2.2 Nitrogen vacancy center

2.2.1 NV^0 center

A defect often found in nitrogen rich type Ib diamond samples after irradiation damage or directly implantation N is the nitrogen vacancy defect centre or NV centre. The NV^0 center is an S = 3/2 spin system consisting of a single vacancy site located adjacent to a nitrogen atom in the diamond lattice (see figure 2.4a). The electronic structure of the NV center enables optical readout and initialization of the spin system through optically detected magnetic resonance (ODMR) [20][23]. It presents a photon excitation energy of 2.56 eV (575 nm) as shown in figure 2.4b.

The optical transition has been found to be between a ^2E ground state and $^2A_2$ excited state. Additionally, an electron spin resonance signal has been detected and attributed to an intermediate $^4A_2$ state. The vacancy centres in diamond can be described by molecular orbitals formed from the dangling bonds of the C atoms associated with the vacancy in addition to orbits of any adjacent impurities.[24]. For the N-vacancy there is a non-degenerate a_1 orbit in the valence band that is generally ignored. In the gap between valence and conduction bands there is a non-degenerate a_1 and a degenerate e state (of A_1 and E symmetry, respectively in C_{3V}) and it is the occupation of these one-electron states that give the electronic levels. For NV^0 there are three electrons (if the one in the valence band is neglected) giving the $^2E(a_1^2e)$ ground state, the $^2A_2(a_1e^2)$ excited state and the intermediate $^4A_2(a_1e^2)$ state. The $^2E - ^2A_2$ emission can be seen from 575 to 700 nm [24]. This discussion is graphically shown in figure 2.5.

2.2.2 NV^- center

The NV center can capture an extra electron to form an NV^-. The local spin states of the NV^- center can be accessed and manipulated optically at a single-site level, making it suitable for quantum information applications. The ground state of the NV^- center in diamond is a spin triplet with an electronic configuration $(a_1^2 e^2)[^3 A_2]$[26]. The electron in the minority spin a_1 state can be optically excited to the unoccupied e state, forming a spin triplet excited state ^3E with a strong zero phonon excitation energy of 1.945 eV (637nm) called the Zero phonon line (ZPL) of the NV^- (see fig.2.5). The optical transitions involve transitions between like-spins and the three spin projections. For $m_s = 0$, $m_s = +1$ and $m_s = -1$ this transitions have equal strength.[26][20][24]. Figure 2.4b shows both the ZPL of the NV^0 and NV^- with their respective excitation wave lengths [7].
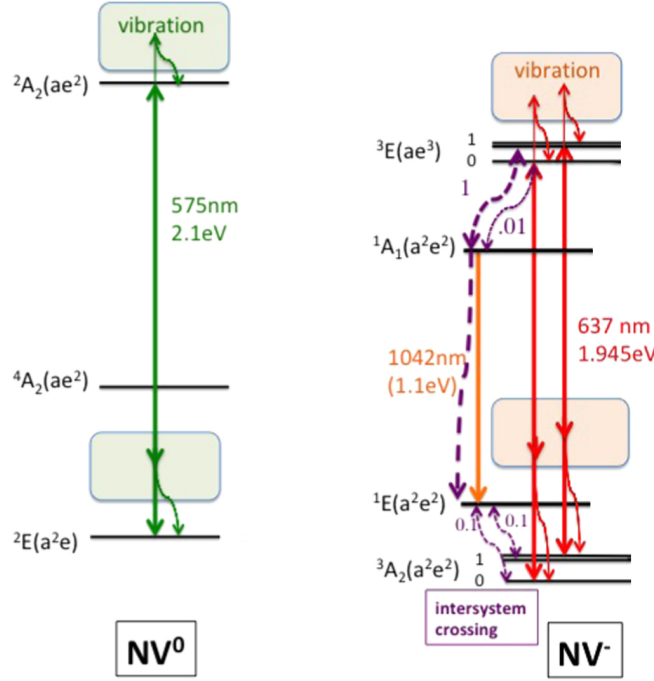
Figure 2.5: Electronic structures of NV centres. Transitions between electronic states are indicated by solid lines (they can be accompanied by vibrations). Non-radiative decay or inter-system crossing is depicted with dashed lines. After [24]

The interconversion between NV^0 and NV^- can be influenced by the power of the laser used and its wavelength. The saturation behaviour of the NV under high power illumination is proportional to the probability to be in NV^-. The fluorescence at varying illumination power was collected by [8] in order to determine saturation curves. The function to fit the measured data and obtain the saturation fluorescence Fl_S and the saturation power I_S is

$$Fl = Fl_s \frac{I}{I + I_S} \tag{2.5}$$

Where *Fl* is the fluorescence and *I* the illumination power. For moderate powers $< 1mW$, this function fits the data very well[8].

2.3 Implantation of ions

Ion implantation is a technique that allows the placement of foreign atoms, ions or other particles in the crystalline structure of a target. By using a particle accelerator, the implanted ions can change the physical, electrical or chemical properties of the material to be doped. Controlling the parameters of the equipment to impinge particles is of capital importance in the whole process.

2.3.1 Energy loss mechanisms

An energetic ion that penetrates into any target loses its energy through scattering events that involve the Coulomb interaction of the ion within the atoms and electrons in the solid. The energy loss determines the final penetration depth of the projectile and the amount of disorder created in the lattice[27]. Each collision is a complicated many body process that can be approximated by sub dividing the Hamiltonian into the ion energy loss of two mechanisms: electronic energy loss (it involves the interaction between the incident ion and electrons of the target) and nuclear energy loss (involves the interaction between the incident ions and the atoms of the host material considered as point charges)[27].

The slowing down of an ion in matter is, therefore, understand through the *stopping power* $\frac{dE}{dT}$, defined as the energy dE lost by an ion traversing a distance dx. Thus:

$$\frac{dE}{dx} = N \int T d\sigma \qquad (2.6)$$

$d\sigma$ being the collision cross section, T the ion energy lost during a collision event, N is the density of scattering centers of the host material. Hence, the stopping cross section ϵ is given by

$$\epsilon = \frac{1}{N} \frac{dE}{dx} = \int T d\sigma \qquad (2.7)$$

The total stopping power due two both nuclear and electronic processes is:

$$\frac{dE}{dx} = \left(\frac{dE}{dx}\right)_e + \left(\frac{dE}{dx}\right)_n$$
$$= N(\epsilon_e + \epsilon_n) \qquad (2.8)$$

Here ϵ_e and ϵ_n are the electronic and nuclear stopping cross sections[27]. There are more detailed approaches that are not considered here.
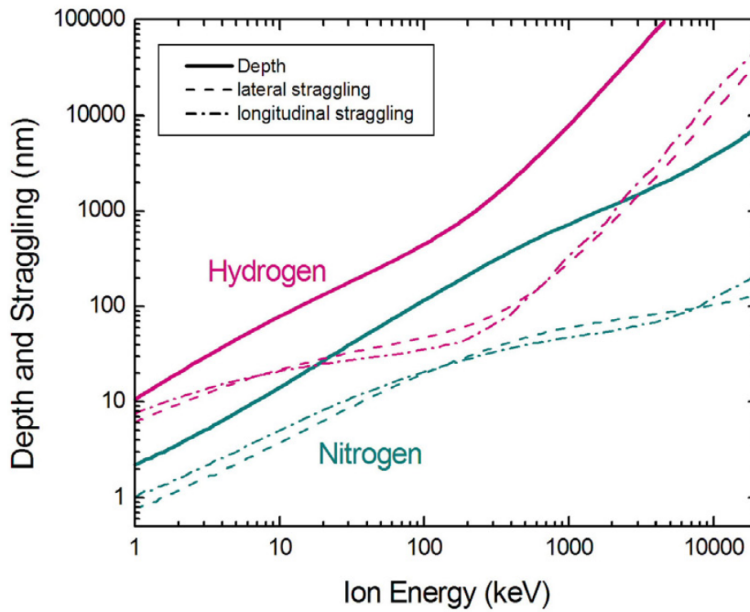
Figure 2.6: Penetration depth and straggle of N and C ions in diamond. Taken from [6] based of simulation on SRIM [30].

2.3.2 Spatial resolution and limiting factors

The spatial resolution is defined as the precision in the final position of an implanted ion in the target material [6], i.e. the volume distribution in which the implanted ions will end up. Of special importance is the lateral resolution, i.e. the implantation depth (and its uncertainty) which is directly related to the kinetic energy of the ion. The lateral resolution is intrinsically limited due to ion-matter interactions. They are treated in the following.

Ion straggle

The ion straggle is defined as the square root of the variance of the ion distribution. It can be regarded as the spread of the ions along the ion beam. It is a complex process which depends on several parameters such as the ion kinetic energy, the nature of the target material, the temperature, the crystal orientation, among others. Ion straggle represents a physical intrinsic limit of the spatial resolution which can be achieved using a particle accelerator. For a kinetic ion propagating into a target material, straggling occurs due to the multiple collisions that the ion experiences at the atoms of the material, in this sense it can be understood as a scattering process of the ions. It results in a broadening of the implantation volume and can be associated to an uncertainty in the final position of each single implanted ion [6][28][29]. Figure 2.6 shows the simulated depth and straggle of ions in diamond as a function of the ion energy for H and N impinging the lattice. For minimizing the struggle, a low energy in the range of 10 keV may be ideally selected.

Ion channelling

The arrangement of atoms in crystals determines the magnitude of incident ion-target-atom interactions. The influence of the crystal lattice on the trajectories of ions penetrating into the crystal is known as channeling. This term visualizes the atomic rows and planes as guides that steer energetic ions along the channels between rows and planes [31]. Ions propagating along low-index crystallographic axes and planes penetrate deeper and produce less defects. Thus channeling leads to a loss of the resolution in the depth direction.

For a given crystal axis of the target material, channeling occurs within an acceptance angle around this axis depending on several parameters such as ion nature, ion energy and sample temperature. The measured depth profiles [6] show that a small part of the implanted ions can penetrate twice deeper as the main implantation depth. Hence the right orientation of the sample, tilted away from any channeling direction, should be chosen in order to minimize this effect.

2.4 Simulations

The program used for the numerical simulations is called SRIM (Stop and Range of Ions in Matter) [30]. It is based on a Monte Carlo algorithm that calculates the interaction of energetic ions with amorphous targets. The program uses several physical approximations to obtain high computational efficiency. One of those is the use of an analytic formula for determining atom-atom collisions and another one is the use of the concept of free-flight-path between collisions (only the significant collisions are evaluated) [28].

In the simulations, the ion energy determines the depth of the region with the maximum vacancies density and the dose determines the vacancies concentration in this region [32]. It is assumed in this work that the ion kinetic energy E is well known and that $\Delta E/E$ is negligible [6].

2.5 Annealing

Annealing is a heat treatment that alters the physical properties of the diamond sample. The first goal of a thermal treatment after any ion implantation process is to heal the radiation defects as much as possible [3], so it is a crucial step in the production of NV centers as can be seen in figure 2.7a. This efficiency is often given as the NV creation yield (the number of observed NV centres with respect to the number of implanted N atoms). It depends mainly on the annealing temperature [19] and on the implantation energy [33][3]. Figure 2.7b shows the typical yield versus energy dependence for two different high purity samples. It shows that the yield increases with the energy, but from 1 to 100 keV, it is only about 10%.
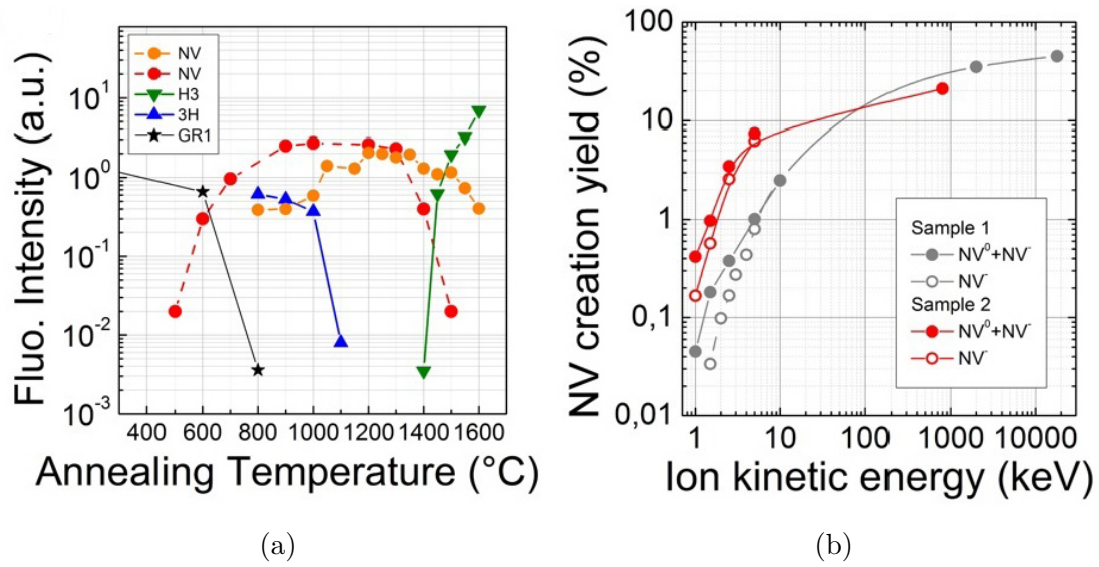
(a)

(b)

Figure 2.7: (a) Temperature dependence of the luminescence for various color centres. The NV centres correspond to implantations of N at $45keV$ and $1 \times 10^{15}cm^{-2}$ (■) and 300 keV and $1 \times 10^{13}cm^{-2}$ (■) (b) Efficiency of creation of NV centers as a function of the implanted kinetic ion energy. Taken from [3].

Chapter 3

Analytical Methods

The description of the experimental methods for the sample preparation (implantation, annealing steps, cleaning with a plasma chamber and solvents) as well as the equipment used for measurements (confocal microscope and spectrometer) are described in the present chapter.

3.1   100kV accelerator.

The implantations required in this work were made using a linear accelerator, the 100 kV implanter, which is equipped with an ion-sputtersource. The accelerator can supply a large variety of ions (except noble gases). The negative ions from the ion source are accelerated to energies starting from a few keV up to 100 keV. The beam is then analyzed by a 90° magnet.

Source of Negative Ions by Cesium Sputtering (SNICS)

It is a sputter ion source capable of delivering anions from a solid sample (cold cathode covered by a Cs layer) by bombarding it with Cs^+ ions. Cesium atoms are heated up in the oven until they form a gas. Inside the chamber there exists a hot conical ionizer maintained at a positive potential. The Cs vapour can stick to the surface of the cathode or to the surface of the ionizer. The Cs gas touching the ionizer gets immediately ionized and so the new Cs^+ ions travel towards the cathode which is maintained at a lower potential. By doing so, the powder of the cathode gets sputtered producing either ions or atoms which then pick up an electron as they pass through the cold, condensed layer of Cs and so produce negative ions. Since the entire ion source is operated below the ground potential and the extractor is kept at high positive potential U_{ext} with respect to the whole ion source, the negative ions are accelerated back and extracted out of the source as a negative ion beam[34][35]. See figure 3.1.
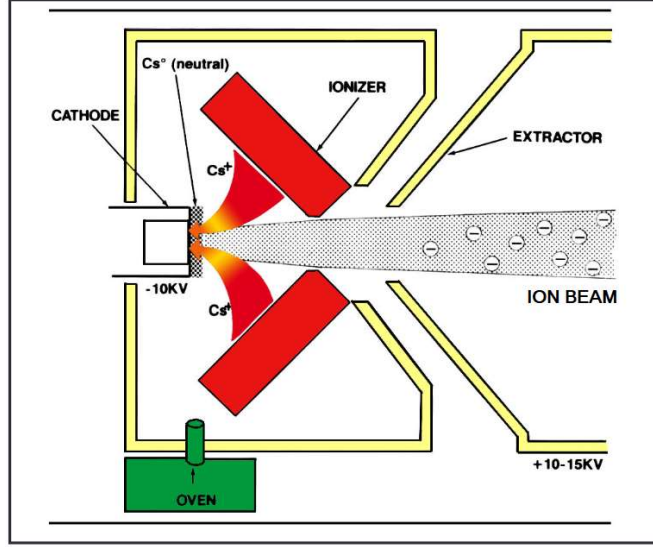
Figure 3.1: SNICS source of the 100 kV Accelerator. Modified from [35]. Cs vapor emerging from the oven is ionized on the ionizer and accelerated towards the cathode, where it removes the cathode powder. A thin layer of Cs on the cathode surface serves as a stripping medium, so that the beam of negatively charged ions thus generated can leave the source (by means of an extractor) with an energy of a few keV.

.

High voltage and magnet

The ion beam leaving the extractor has a kinetic energy between 5 and 10 keV. It is further accelerated by means of a set up of ring electrodes to its desired energy (up to $U_{HV} = 100\,\text{kV}$), as shown schematically in figure 3.2. When leaving this section, the particles have an energy of $E = qU_{tot}$, the total voltage being $U_{tot} = U_{cato} + U_{ext} + U_{HV}$ [36]. The beam at this point contains ions of other species besides the desired one, since the cathode material contains impurities. Thus a magnet providing a magnetic field at 90° of the direction of the electric field serves a mass separator by means of the Lorenz force [36]. (see fig. 3.2).

The magnetic flux density B_{mag} in the 90° magnet is approximately proportional to the flowing current I_{mag}, as long as the iron core of the magnet is not saturated. The proportionality factor results from the maximum current $I_{max} = 153A$ and the resulting magnetic flux density $B_{max} = 1.05T$. The filtered masses $m(I_{mag})$ now result from the condition of a stable trajectory of the ions (charge q) with a radius of curvature of the magnet of $R = 0.5m$ [37]:

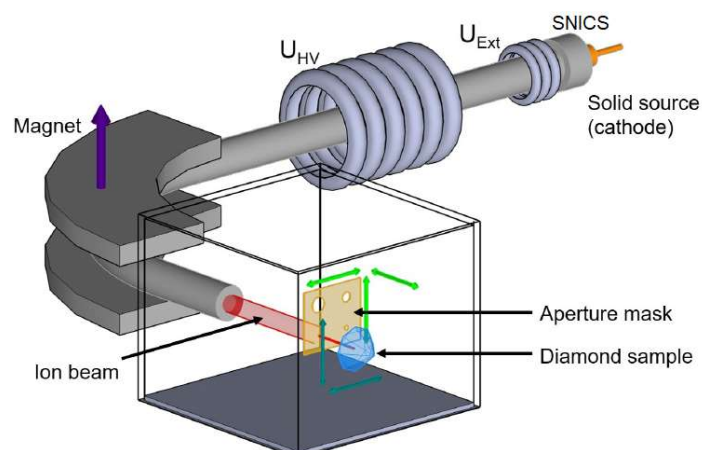$$m(I_{mag}) = \frac{I_{mag}^2 R^2 B_{max}^2 q}{2U I_{max}^2} \tag{3.1}$$

Figure 3.2: Diagram of 100 kV accelerator. The ions from the extractor are accelerated linearly by means of a high voltage U_H towards a magnet that bends the direction of the ion beam and selects the specific required ion. The collimated beam further hits the aperture mask and finally reaches the diamond. Taken from [3].

As described before, the SNICS source only produces negative ions. N cannot be easily negatively charged because it is very unstable [38], therefore it can only be implanted using compounds such as $(CN)^-$ and $(BN)^-$. Finally, the collimated beam hits a mask (see fig. 3.3) that allows ions to pass only in the desired area of implantation.

3.2 High temperature oven

For the annealing steps an oven that can reach a temperature of $2000\,^{\circ}\text{C}$ was used. The vacuum is realized by a pump that allows a pressure of $10^{-6}mbar$. Therefore the oxygen that could be in the graphite heating chamber is pumped out, which prevents any oxidation of the diamond when reaching high temperatures. In the figure 3.4, the lid of the oven is lifted and the graphite chamber can be seen. The sample is be placed inside this chamber.

3.3 Plasma Chamber

A low pressure plasma equipment of the brand *Diener* is used for removing organic impurities from the surface of the diamond (including C from graphitization points). An energetic plasma is created in the chamber (see fig. 3.5) from oxygen by using a high frequency voltage. The plasma chamber comprises the following components[39] (see fig. 3.6):

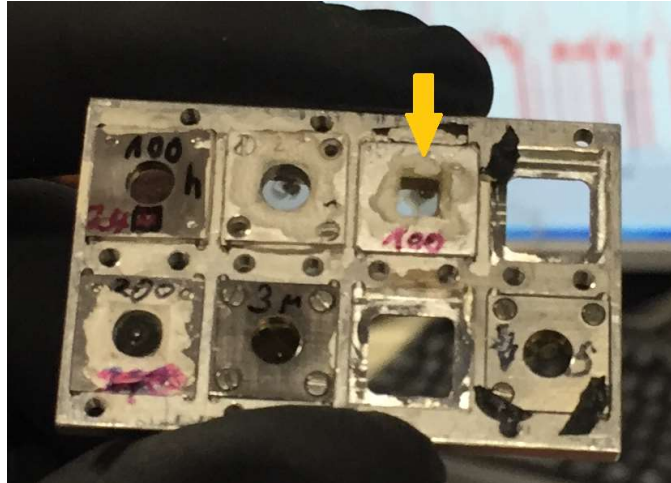Figure 3.3: Masks used for the implantations, the arrow shows the $100\,\mu\text{m} \times 100\,\mu\text{m}$ mask used to implant the carbon and nitrogen ions.
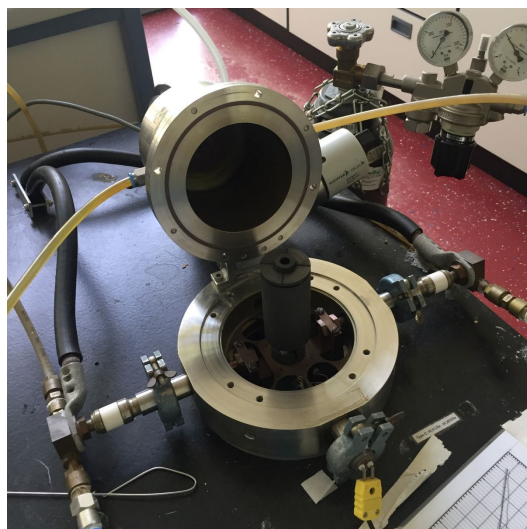

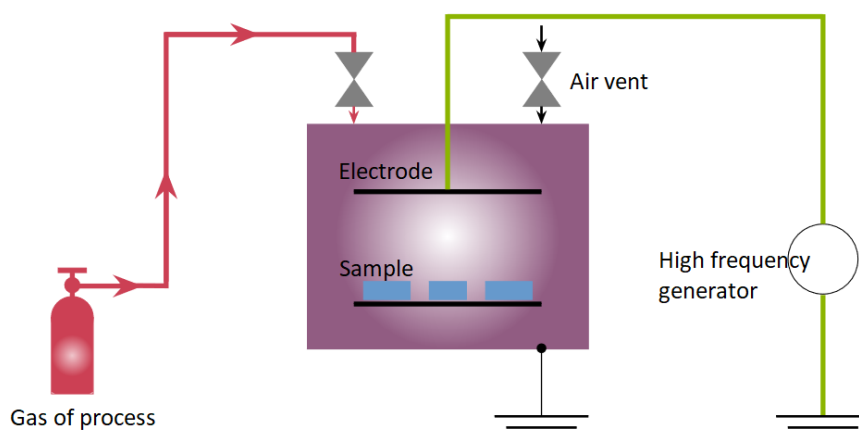Figure 3.4: High temperature oven used to anneal the sample.

Figure 3.5: Diagram of the plasma Chamber. The gas enters the chamber and is ionized and further transformed into plasma by high frequency coupling. The plasma particles hit the surface of the sample and remove the impurities of the surface. Modified from [36], based on [39].

Recipient or chamber. The recipient is a vessel or chamber where a plasma process takes place. It needs to be fabricated from stainless steel, a material which resists the plasma processes executed inside.

Vacuum pump. It is an oil lubricated rotary vane pump that can achieve pressures of about $10^{-3}mbar$.

Plasma generator. It is the unit providing the alternating voltage for the excitation of the plasma. The generator provides a low frequency of $40\,kHz$ and the power can be chosen between 0 and $200\,W$.

Control panel. It controls the vacuum pump, the supply of the process gas, time and power setting, generator and ventilation.

Electrodes. Two electrodes are arranged around the glass cylinder and are connected to a high-frequency generator. An electric field is established when being charged by an electric voltage. The desired gas is fed into the cylinder and the generator generates a plasma by capacitive-electrical excitation. By this method a homogeneous plasma in a large volume can be generated [39][37].

Figure 3.7: Home made confocal microscope.

Figure 3.6: Plasma chamber. Note the bottle of oxygen at the left of the picture.

Once the sample is prepared, or it is in an intermediate step of preparation, the usage of the confocal microscope and the build in spectrometer is required.

3.4   Confocal microscope

A confocal laser scanning microscope (CLSM) allows to obtain an image from a prescribed section of a thick translucent object, without the presence of out-of-focus information from surrounding planes [40]. The confocal principle fulfils this requirement and at the same time provides enhanced lateral resolution. Light from the specimen is focused through a small aperture (pin hole), located in the conjugated plane of the sample and the image. This ensures that only the light contributing to the image formation can pass through the aperture and form an image. Therefore information is obtained only from one particular level of the specimen, as seen in figure 3.8. Furthermore, only light from a very small volume
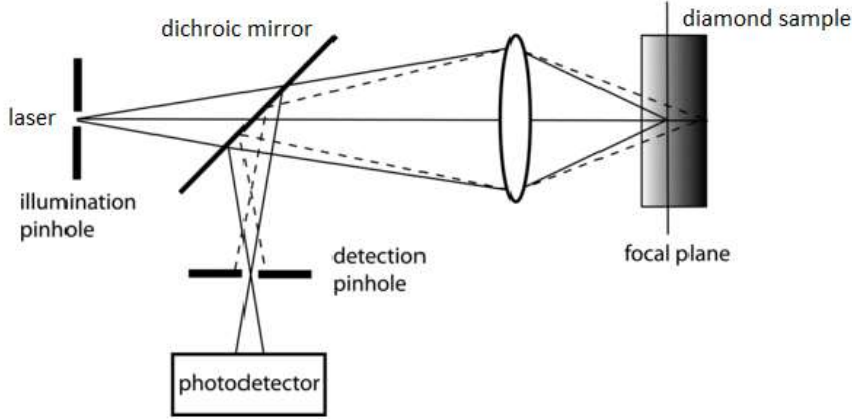
Figure 3.8: In a confocal optical system, light originating from a luminescent object placed in the focal plane is directed towards a dichroic mirror which focus the light on a pinhole. Almost all of this light passes through the pinhole and reaches the photodetector. Light from regions of the object lying in planes away from focus arrives as a defocused spot at the pinhole.[41] The pinhole physically blocks this light so it can not reach the photodetector, which therefore measures almost only the signal focused indeed in the focal plane and avoids the defocused planes. After [41].

around the focal point in the sample reaches the detector. As a result, images with very high contrast can be created but they should be scanned point by point. Therefore the sample is located on a movable holder and the intensity of the fluorescence is measured point by point [36]. The resolution of a confocal microscope is determined by the confocal illumination and detection volume. Both are described by a point spread function (PSF) h_{Illm} or h_{Det}. The total PSF h_{Tot} behind the pinhole is:

$$h_{Tot} = h_{Ill} \times h_{Det} \tag{3.2}$$

Which leads to the equations for lateral and axial resolutions [42][36]:

$$r_{lat} = \frac{0.44\lambda}{NA}$$
$$r_{axial} = \frac{1.5n\lambda}{NA^2} \tag{3.3}$$

Where NA is the numerical aperture of the lens used in the objective, n the diffraction index of air or other media, λ the excitation wavelength [43].

Experimental Setup

A Nd:YAG (neodymium-doped yttrium aluminum garnet) laser provides a wavelength of $\lambda = 532\,\text{nm}$ which through a system of lenses and beam splitters (see fig. 3.9) arrives to a partially transparent mirror. This mirror reflects the laser
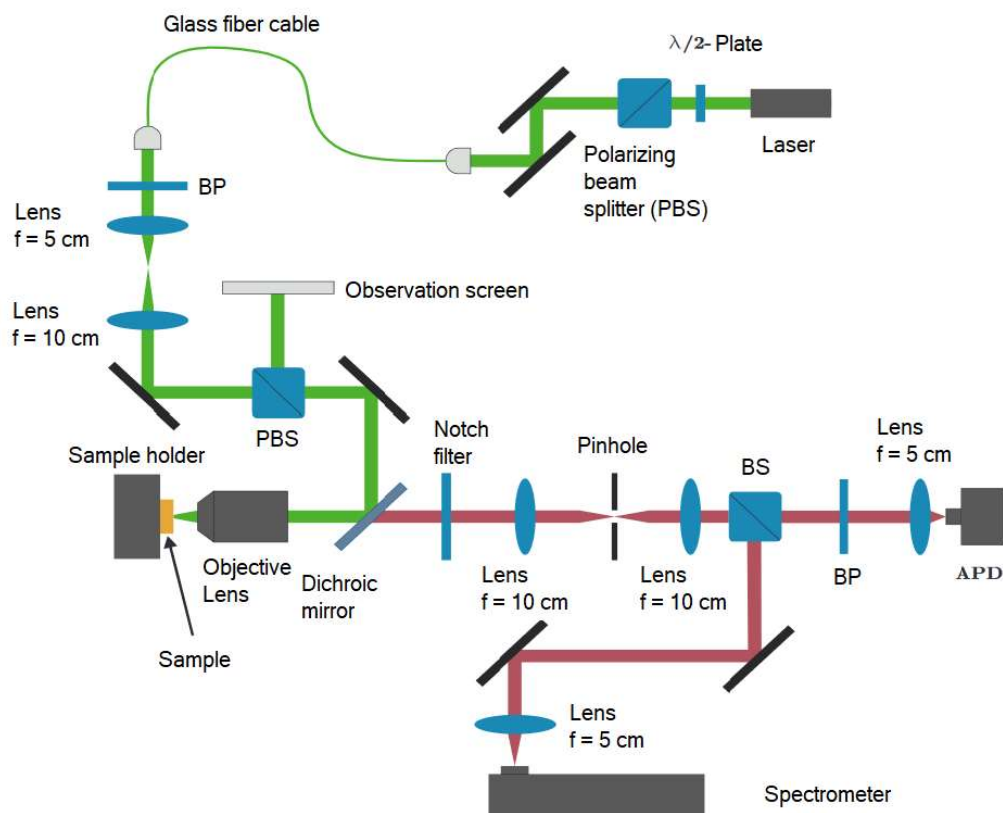
Figure 3.9: Diagram of the set up of CLSM taken from [36]. Parts of the configuration as well as the place of the filters can be changed depending on the experiment.

through the objective (see fig. 3.8) into the sample. The sample gets excited and emits fluorescent light. It passes through a notch filter (which filters out the reflexions of the 532 nm laser) towards a pinhole (confocal principle). From here, the fluorescence is detected either by a CCD-based spectrometer (Horiba Jobin Yvon GmbH) or arrives -through a band pass (BP) filter-, to a photodetector (Excelitas SPCM-AQRH) which is an avalanche photo diode (APD) type used for single-photon detection via a single photon counting module (SPCM).

Individual photons in the wavelength range from 400 nm to 1060 nm can be detected. The detection efficiency specified by the manufacturer is dependent on the wavelength, but is a maximum of 65% at a wavelength of 650 nm [44]. The dead time of the device is 50 ns [36].

Altogether, two factors contribute to the spatial resolution: the volume area excited by the laser and the depth plane let through the pinhole. A spatially resolved distribution of the fluorescence intensity of the sample can also be created by simultaneously controlling the piezo stage and recording the diode count rate

using a program [43].

Grating spectrometer

Spectra of the sample's fluorescence can be recorded at any point in the scan field by means of a grating spectrometer, built in the confocal set up. The beam of fluorescence arrives at a slit-shaped entry and is directed towards a grating by means of a concave mirror. The light hits the grooves of the grating and gets diffracted. This light reaches a CCD (charge coupled device) detector.

Page intentionally left blank.

Chapter 4

Steps of measurement

As the sample preparation and the experimental methods of measurement were described in chapter 3, this chapter focuses on the design of the experiment as well as explaining the actual sequence of steps.

4.1 Preliminary preparation

Design of the experiment

The creation yield of NV centers after implantation of various species of carbon (C_1^{1-} to C_6^{1-}) is to be determined in regions of the diamond where dopants S, B, O, P were implanted. The differences in the creation yield depending on the carbon molecule number are then to be analysed as well as the influence of the dopant type (acceptor or donor) or the absence of it.

The premise of this thesis is that the spatial distribution of vacancies will be denser when making impinge carbon molecules as when implanting single carbon atoms (for a constant fluence) in the diamond lattice. Therefore the NV creation yield is potentially higher because of the higher number of vacancies in the surrounding. Figure 4.1 shows schematically how the distance between vacancies produced by single C_1^-s is expected to be greater than the one when higher carbon molecules (C_2^- to C_6^-) are implanted.

As an intermediate step in this experiment, the creation of vacancies for Boron and Sulfur doping in selected sites of implantation is also studied before the final annealing step. The implantation energies for B and S were 10.1 and 30 keV respectively (see table 4.1). Such energies were chosen to achieve an overlap between the created vacancies and dopant's level as explained in section 4.1.3. The implantation of C_1^{1-} at 48 and 80 keV in B and S doping areas will create the maximum concentration of vacancies deeper than the levels at which the dopants are expected to reach its maximum concentration and therefore this potential lack of overlap will give hints of the mobility of the vacancies after annealing.
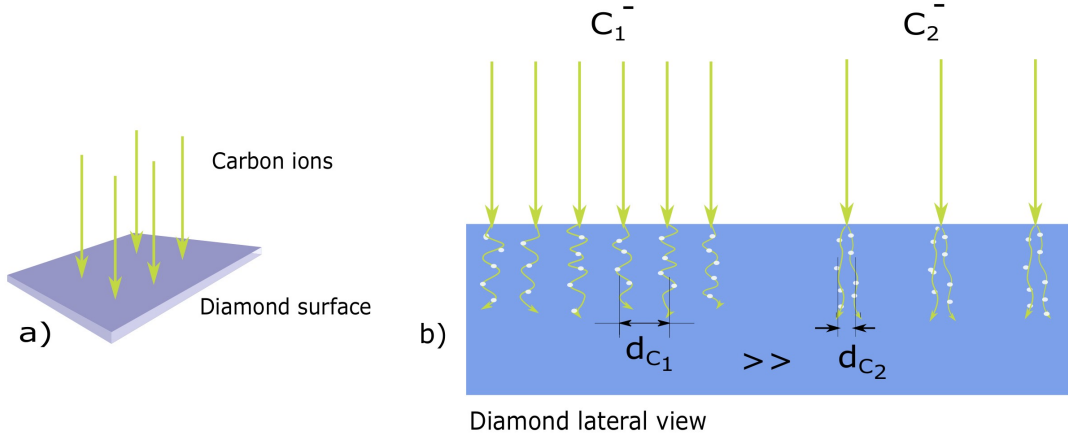
Figure 4.1: a) General scheme for implanting carbon ions in a diamond. b) Expected behaviour of the Vacancy distances when implanting single carbon ions C_1^- as when implanting $(C-C)^-$ molecules using the same fluence in both cases. The vacancies are represented here with white dots.

Sample selection

For the present work two samples grown by the manufacturer [45] with a Chemical Vapour Deposition (CVD) synthesis process, faces in the plane {100}, laser cut edges were used. The first one is an optical grade diamond polished by one side with thickness of $0.3 \pm 0.05mm$. Its width is $2.60 \times 2.60mm$. The nitrogen concentration is < 1 ppm and the Boron Concentration is $< 0.05ppm$. This sample was discarded after all of the implantations, because of its high-density of intrinsic N does not allow to control over single NV centers as already noted in [46].

The second one is a high purity Single Crystal Electronic (ELSC) grade diamond material with respect to point defects, with a low N and NV centre density less than 5 ppb Nitrogen and -according to the manufacturer [45]- typically has less than 0.03 ppb NV concentration. The concentration of Boron is less than 1 ppb, its width is $2.00 \times 2.00mm$ and polished on both sides.

Simulations using SRIM

To determine optimal energies for the ion implantation, numerical simulations were carried out using the software SRIM [30].

There exists a compromise between 1) the energy of the ion implantation 2) the desired dose, 3) the optimal penetration depth of the ions and, 4) the depth at which a greater number of vacancies will be created. Additionally these factors are constrained to the maximum energy the available particle accelerator can achieve which is 100 kV. All of the above conditions were found to be fulfilled at around a

Ion	Selected Dose	Simulated Energy	Penetration depth of max. number of ions	Depth maximum number of vacancies	Density at 20 nm
	$ions/cm^2$	keV	nm	nm	$ions/cm^3$
			Dopants		
N^-	5.00×10^{11}	14.2	20.0		2.5×10^{17}
S^-	1.00×10^{12}	30	20.4		4.9×10^{17}
O^-	1.00×10^{12}	15.6	20.0		5.00×10^{17}
B^-	1.00×10^{12}	10.1	20.0		5.00×10^{17}
P^-	1.00×10^{12}	26.8	20.0		5.00×10^{17}
			Ions to produce vacancies		
C^-	3.00×10^{11}	16		18.0	
C_2^-	1.50×10^{11}	32		18.0	
C_3^-	1.00×10^{11}	48		18.0	
C_4^-	7.50×10^{11}	64		18.0	
C_5^-	6.00×10^{10}	80		18.0	
C_6^-	5.00×10^{10}	96		18.0	

Table 4.1: Results of simulations using software SRIM. The maximum number of vacancies should be created at a penetration depth in which the higher concentration of dopants is expected.

depth of 20 nm. The table 4.1 summarises the parameters obtained after various attempts to conceal this variables. An example of the multiple simulations carried out can be seen in figure 4.2.

The simulated overlap between expected vacancies and position of the implanted ions in the diamond lattice is shown in figures 4.3a and 4.3b. At around 18 nm from the surface the majority of vacancies will be created. At this level the mean number of vancacies created is simulated to be 80 vac/ion. Thus despite its migration through the diamond lattice after annealing, there will exist enough number of vacancies for NV centers to be created. This fact is also true when a higher energy (80 KeV) is used for the carbon implantation. Here a big number of vacancies will be created at the level in which the substitutional atoms of B and S are located as seen in figure 4.4.

4.2 Sequence of measurements

The figure 4.5 shows the operational procedure for this work.

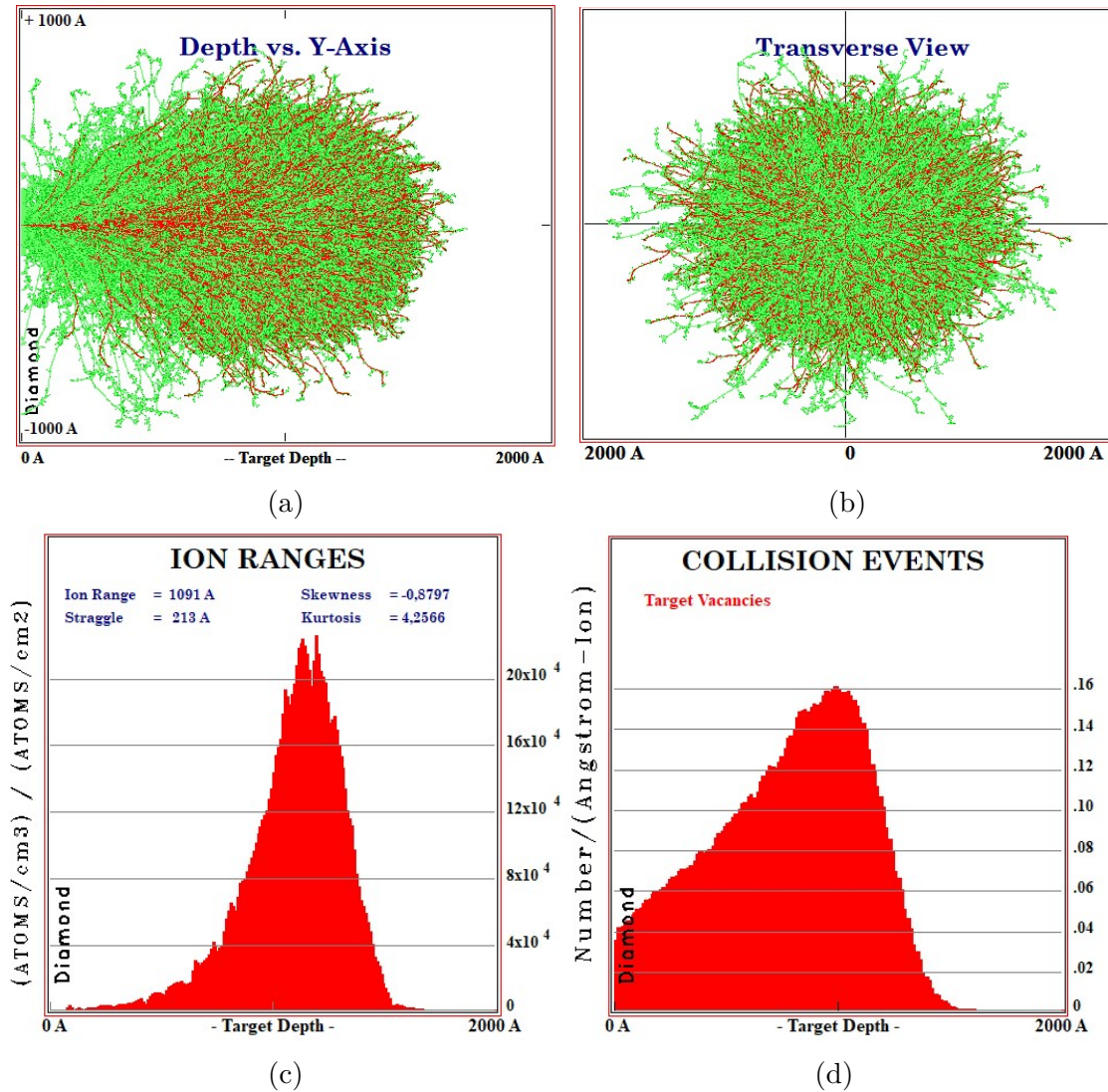(a)   (b)

(c)   (d)

Figure 4.2: Example of simulations using SRIM [30] for C_1^{-1} at 80 keV. (a) Lateral view of the ions impinging the crystal Lattice. (b) Transverse view. (c) The maximum number of ions penetrate about 1100 angstroms. (d) The damage of the ions in the diamond lattice is expected to be at a depth of 1000 Angstroms.
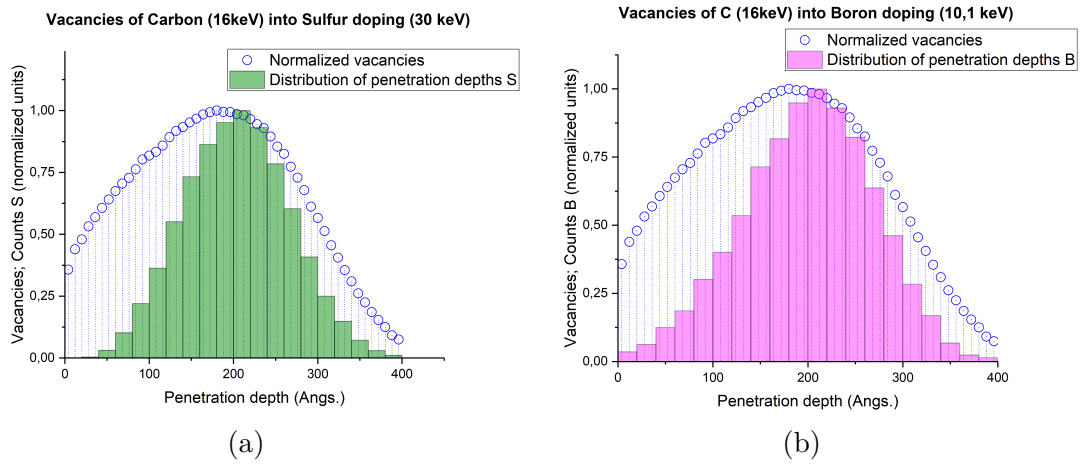
(a)   (b)

Figure 4.3: Simulation of the overlap between vacancies created by implantation of C_1^- and the penetration depth distribution of dopants. In 4.3a Sulfur is presented in ■ and in 4.3b Boron is presented in ■.
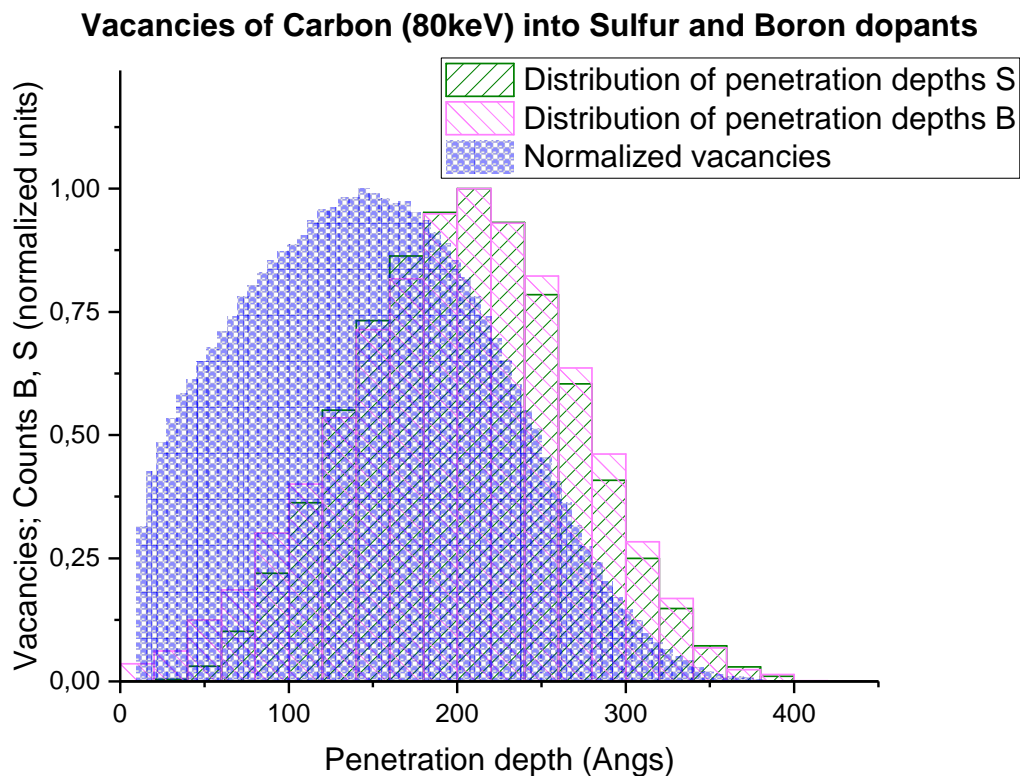

Figure 4.4: Overlap of vacancies created by implantation of C_1^- at $80keV$ and B and S. Note despite of the bigger energy, there exist a good overlapping.
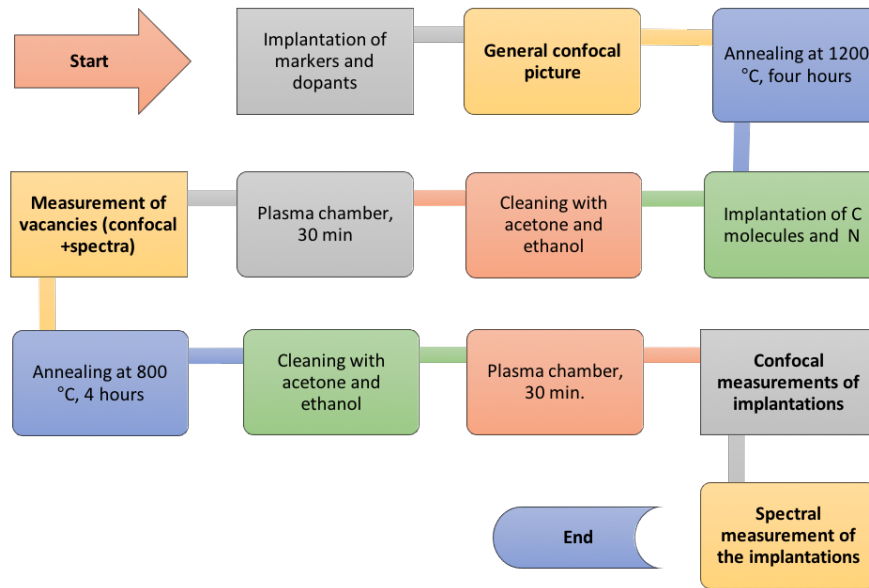
Figure 4.5: Sequence of the steps done in this work.

Implantation of markers and dopants

Nine graphitization points of $50\,\mu$m of diameter were implanted in the diamond sample so the identification of the regions of interest is easily performed when using the confocal microscope. The dopants (S, B, O, P) were implanted using an aperture of $240 \times 240\mu m^2$ with each marker located at the center, as seen in figure 4.6. The doses of implantation can be seen in table 4.1.
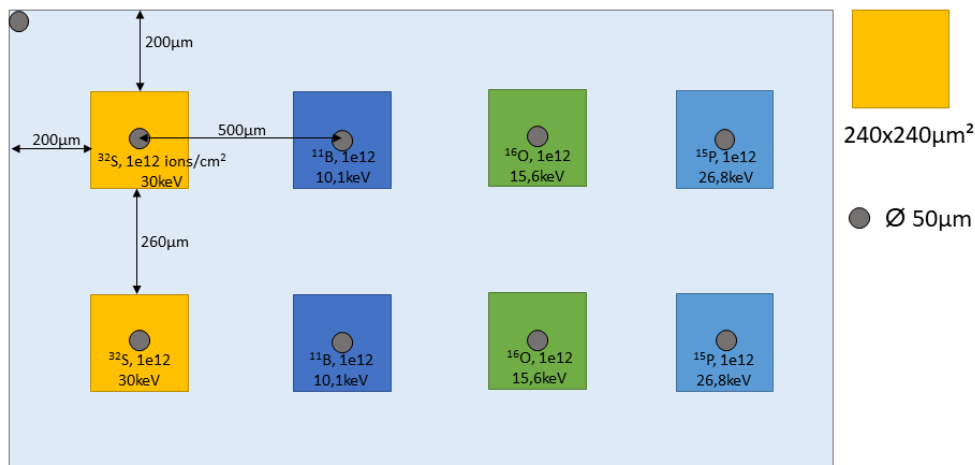

Figure 4.6: Diagram showing the distribution of dopants along the diamond. Sulfur ▮, Boron ▮, Oxigen ▮, Phosphor ▮. The graphitization point at the upper left avoids to flip involuntary the sample.

The sample was first annealed at a temperature of 1200 °C for four hours in a vacuum pressure of $6.8 \times 10^{-8} mBar$.

Implantation of N^- and C_n^-.

A region of $100 \times 100 \ \mu m^2$ of N^- with a fluence of 5×10^{11} was implanted in every corner of the dopant as seen in figure 4.7. Regions of $100 \times 100 \mu m^2$ of different single ions and molecular ions of C were implanted (totally overlapping the nitrogen areas) as shown in figure 4.7 The used fluences can be seen in the same figure and in the table 4.1.
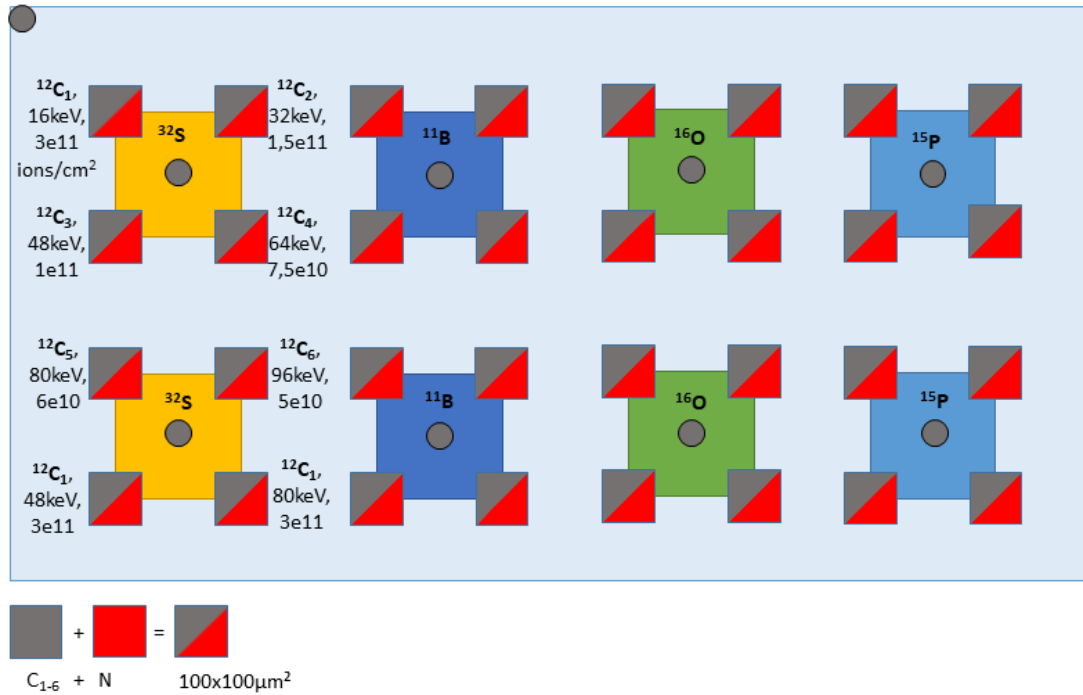

Figure 4.7: Location of C_1^- to C_6^-. Note the N and C molecules overlap completely each other. The labels of the C and N atoms, as well as the energies and fluences are shown only for dopant S (first column), nevertheless the same values are valid for the other dopants.

As it can be seen in the previous figure, the above implantation design allows to have an overlap of the N with C ions which at the same time is located inside and outside the doping areas. Therefore, a further background correction can be performed.

To ensure the sample is clean enough, it was put in a ultrasonic bath of acetone for 10 minutes, followed by a 10 minutes ultrasonic bath of ethanol.

Vacancy measurements

The creation of vacancy centers V^0 was measured before the final annealing step. The vacancies are identified by the presence of the General Radiation (GR1) peak at 741 nm. They are produced by the collisions of the N and C_N^- ions along its path through the diamond [3]. In order to identify the different regions of interest the nomenclature shown in figure 4.8 is adopted.
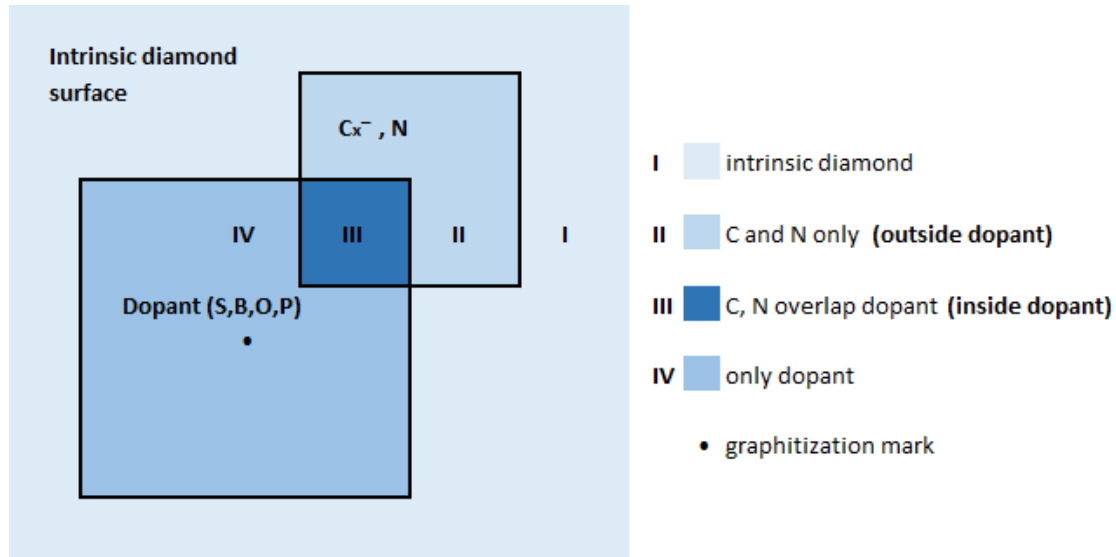

Figure 4.8: Schematic location of the implanted and not implanted areas in the diamond. The dot symbol • in the center of the doping area represents the graphitization mark used only for purposes of orientation while using the confocal microscope.

Confocal and Spectral measurements

The measurements were conducted in a home made laser scanning confocal microscope, with an air objective ($\times 100$, NA=0.95) and a laser excitation of 532nm. The diamond was placed in the sample holder of the confocal microscope set up and approached to the objective lens, at first manually and second by means of a piezo motor until its surface is in the focal plane of the confocal microscope as described in the previous chapter. The laser reflection was suppressed by a suitable *notch* filter and different optical filters were used to select the wished fluorescence band of neutral vacancies V^0 (GR1 centre, ZPL at 741nm) [47]. The sample was scanned using the CSLM set up in the area of B with implantation of C_6 and $C_1@80keV$. Each area of implantation was divided in four regions (I, II, III and IV as seen in figure 4.8) in order to perform later background correction. Accumulated spectra were also taken using the built in spectrometer. The parameters used are shown in table 4.2.

Parameter	value	unit
Notch filter	532	nm
Filter in front of the APD No.1	650LP	nm
Laser power	4.9	mW
Type of polarization	–	circular
Accumulation time	45	min
Resolution	1000	pixels
Size of the image	20×20	$\mu m \times \mu m$

Table 4.2: Parameters for measuring vacancies in B doped diamond and outside doping at C_1@$80 keV$ and C_6

For the measurements of Sulphur in the region of C_6^- implantation, the same parameters as shown in table 4.2 were used, with the exception of the filter in front of the APDs that here was chosen to be 775/50BP.

Background correction of the spectra

The measurements in the regions **I, II, III, IV** as described in figure 4.8 were used for a background correction which is used along all of this thesis: The region ***outside doping*** is obtained by the subtraction of the sub-regions **II-I** and corresponds to the actual fluorescence due to the implantations of N and C ions that do not overlap the doping area. Similarly the region ***inside doping*** is realized as the subtraction of the sub-regions **III-IV** and corresponds to the actual fluorescence due to N and C ions implantations that do overlap the doping area.

Measurement of NV centers.

The influence of the dopants S, O, P (donors) and B (acceptor) over the creation yield of *NV* centres was analysed by implanting an equal dose (4.1) of ions C_1^- to C_6^- in regions inside and outside the diamond doped areas according to figures 4.7 and 4.8.

Second Annealing step

The creation of NV centres by N ion implantation requires an annealing step to ensure the positioning of the N atom in a substitutional place and the diffusion of vacancies until one of them is captured to form the NV centre [3]. The annealing was done at $800\,^\circ$C and vacuum pressure of $4.7 \times 10^{-5} mbar$ during four hours. Additionally, the sample was cleaned with an ultrasonic bath of acetone and ethanol to get rid of environmental impurities that could be present in the surface and are not strongly adsorbed to the surface.

Plasma chamber

The diamond was further placed for 30 minutes in the plasma chamber with oxygen as process gas in order to remove the adsorbed organic impurities possibly present in the surface of the sample [39]. This process additionally can activate the shallow NV centers that could exist in the dark state as noted in [48].

Confocal and Spectral measurements

In this step the NV centres (ZPL of NV^0 at 575 nm and ZPL of NV^- at 638 nm) [47] were studied. The sample was approached to the objective lens by means of a piezo motor mounted in the sample holder. This was done in order to make the laser exciting the NV centers at the surface of the diamond and to further record its fluorescence. The parameters used in the confocal and spectrometer set ups are shown in table 4.3. The definitions of the different areas to be scanned are the same as for the case of vacancies (see fig. 4.8), and they were used -as already noted- to perform the background correction of the spectra.

Parameter	value	unit
Notch filter	532	nm
Filter in front of APD N0. 1	594LP	nm
Laser power	1.1	mW
Type of polarization	–	circular
Accumulation time	2	min
Resolution	200	pixels
Size of the image	20×20	$\mu m \times \mu m$

Table 4.3: Parameters for the scanning of NV centers

Chapter 5

Results and discussion

The results of the measurements described in the previous chapter are presented here and the main findings regarding the creation of neutrally vacancys V^0, NV^0 and NV^- centres are discussed for two types of dopants: an acceptor (B) and a donor (S). The yield of NV centers is attempted to be calculated with the methodology presented in [47].

5.1 Neutrally charged vacancy

5.1.1 V^0 in Boron doping

The background corrected spectrum corresponding to the implantation of C_6^- is shown in figure 5.1 for B. It is known in a diamond with low N concentration, almost all of the vacancies are in the neutrally charged V^0 state [49], nevertheless the peak corresponding to the ZPL of the GR1 center is higher in intensity for the diamond doped area (thus there exists here more vacancies) as compared to the area outside the doping. This is explained because by doping the diamond with an acceptor (B), the charge state of the vacancies is stabilized[3] in a neutral state. The same tendency can be seen for the implantation of C_1^- at 80 keV (figure 5.2). The $y - axis$ scale presented in this work is always linear unless the contrary is specified. It should also be noted that the negatively vacancy V^- (ND1 at 393.7 nm or 3.149 eV [50]) was not possible to measure due to the range of the available spectrometer.
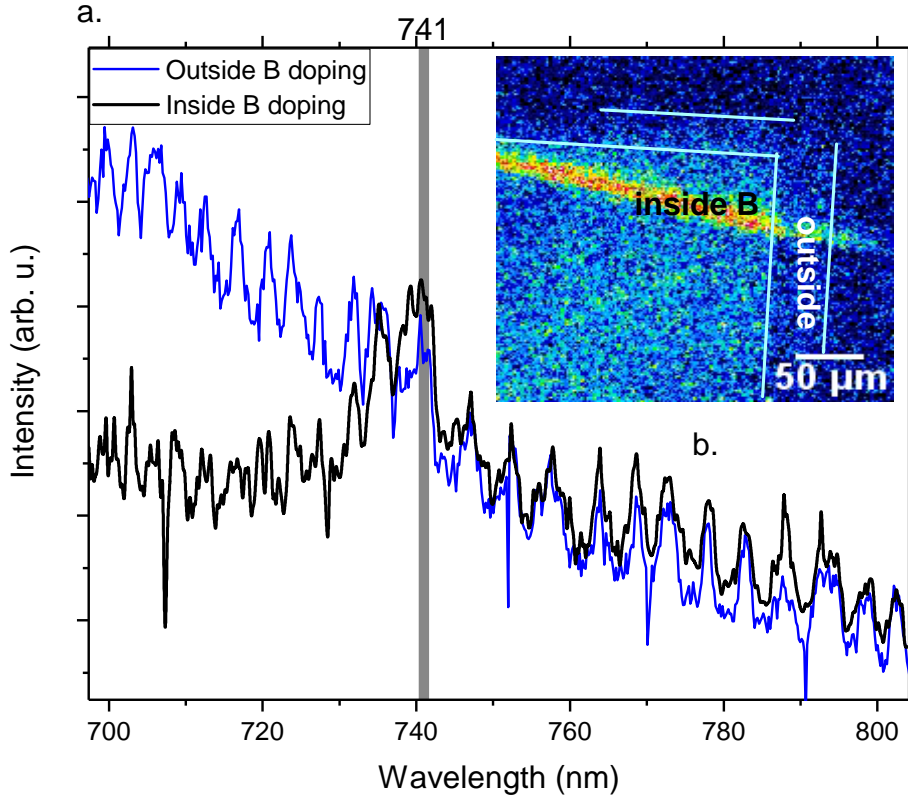
Figure 5.1: **a.** C_6^- implantation inside ■ and outside B ■ doping region after background correction. The ZPL of the GR1 center is shown at 741 nm. **b.** (insert) Confocal image showing the higher fluorescence inside the doping area as compared with the external region. Guiding lines were added. The tilted structure crossing the sample is an artifact of measurement.

The result described above is additionally confirmed by the analysis of the background corrected confocal images with the software ImageJ [51]. It was found that the fluorescence in the Boron doped diamond is 1,37 times higher for C_6^- implantation and 1,79 times higher for C_1^- at 80 keV implantation as compared with the areas of the sample without any extrinsic doping. A similar result was found by [47]. It is to be noted here the units of the intensity are arbitrary so only ratio analysis can be done.
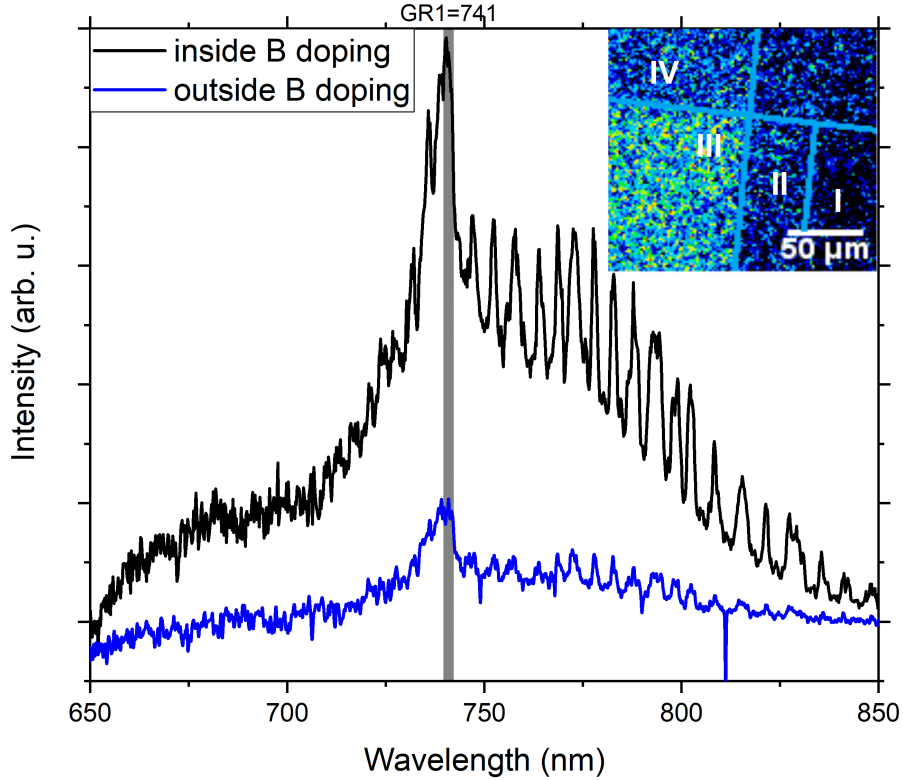
Figure 5.2: C_1^- at 80 keV in the boron region. The peaks corresponding to the ZPL of the GR1 center (741 nm) are clearly shown. The intensity is lower outside the B doped diamond ■, as expected. **Inset** Confocal image showing four regions already defined in figure 4.8. A higher fluorescence (higher number of V^0) is easily shown in the region **III** if compared with the region **II**.

5.1.2 V^0 in Sulphur doping

The results of the previous section regarding the abundance of vacancies are inverted when using sulphur instead of boron as dopant. The region with higher number of vacancies is now located outside the sulfur doped diamond (this corresponds to the intrinsic diamond with a low concentration of N and high concentration of V^0 as described by ref. [50]). In addition a less number of vacancies is found inside sulphur doped diamond, because the negative charges of the donor contribute to change the V^0 to a negatively charged state V^- that does not sum up to the recorded fluorescence. The creation of vacancies was studied for the sulphur doping around the implantation of C_6^- as seen in figure 5.3.
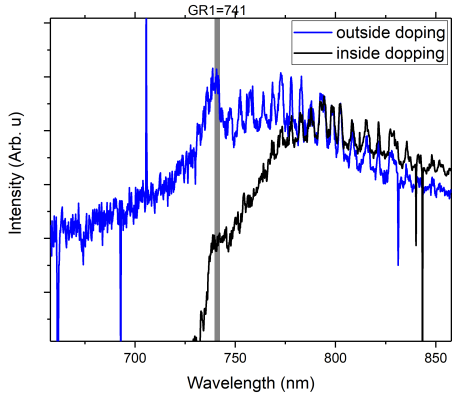
Figure 5.3: **a.** C_6^- implantation inside and outside S doping region. The GR1 peak (see color ■) is higher outside the S doping. As always the y-axis scale is linear.
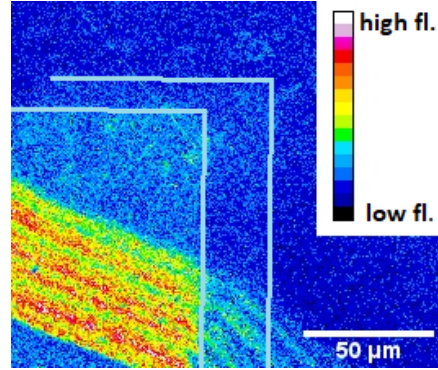

Figure 5.4: Confocal image corresponding to the spectra in fig. 5.3. Guiding lines were drawn to show the separation of the different regions.

A qualitative analysis of the confocal image 5.4 leads to determine the fluorescence regarding the V^0 is, as expected, about 2,71 times higher outside the S-doped diamond. This result means that in the S-doped region there exists vacancies which have the same charge state and therefore a Coulomb repulsion [3] is realized between them. Such repulsion will prevent the formation of di-vacancies after annealing, which in turn helps to increase the yield of NV centers by hinging the creation of other undesired centres as will be shown in the next section. A more quantitative analysis was not possible, since at this point there exist already *NV* centers (probably activated due to the use of the plasma chamber [48], or due to the low N concentration present in the intrinsic bare diamond at the moment of the first annealing step) that are summing up to the measured intensity even though the sample was not yet annealed for the second time.

5.2 Creation of NV^0 and NV^- centers.

Unfortunately the quality of the diamond in the region of interest corresponding to dopants O and P does not allow to perform further measurements. In the following, only the S (first column) and B (second column) doping (see figure 5.5) will be discussed.
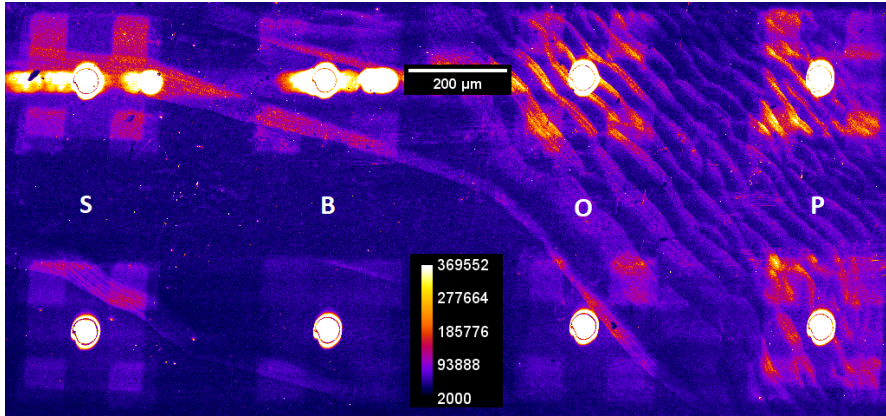
Figure 5.5: 1200×1200 pixels resolution confocal image taken after all of the programmed implantation and annealing steps as described in chapter four. The columns of dopants from left to right are sulfur, boron, oxygen and phosphorous. Note the clear overlaps in the sulphur region (first column). The quality of the diamond from the middle to the right did not allow proper measurements. The numerical and the color scales are placed in the middle of the picture for the sake of visualisation.

5.2.1 NV^0 and NV^- centers in Sulphur doping

The influence of the S doping on the creation yield of NV centers is discussed in this section. The spectra taken after background correction are shown in the figure 5.6 (for the case of C_5^- and C_6^- a background correction was not done because of the presence of artifacts of measurement in the diamond which impeded the correct subtraction of the background). It can be clearly seen in figures 5.6a to 5.6d that a higher intensity of the NV^- centers, expressed through the ZPL peak of NV^- at 638 nm, is given for the regions in which the carbon ion implantation overlaps the S doped diamond (marked with the color ■). This is explained because the negative charge state requires an electron from a donor in the diamond lattice, as pointed out by [24], therefore the unpaired electron in the donor S may charge the vacancy site. In addition, the NV centre's yield is also favoured by the Coulomb repulsion of the V^- vacancies. Neither the ZPL nor the phonon side bands of the NV^0 appeared in the measurements. It is also to be noted that an inter-conversion between NV^0 and NV^- can be optically induced by selecting an appropriate laser power [8]. Nevertheless the important finding here is the high yield of NV^- centres driven by the presence of sulfur as dopant [3].
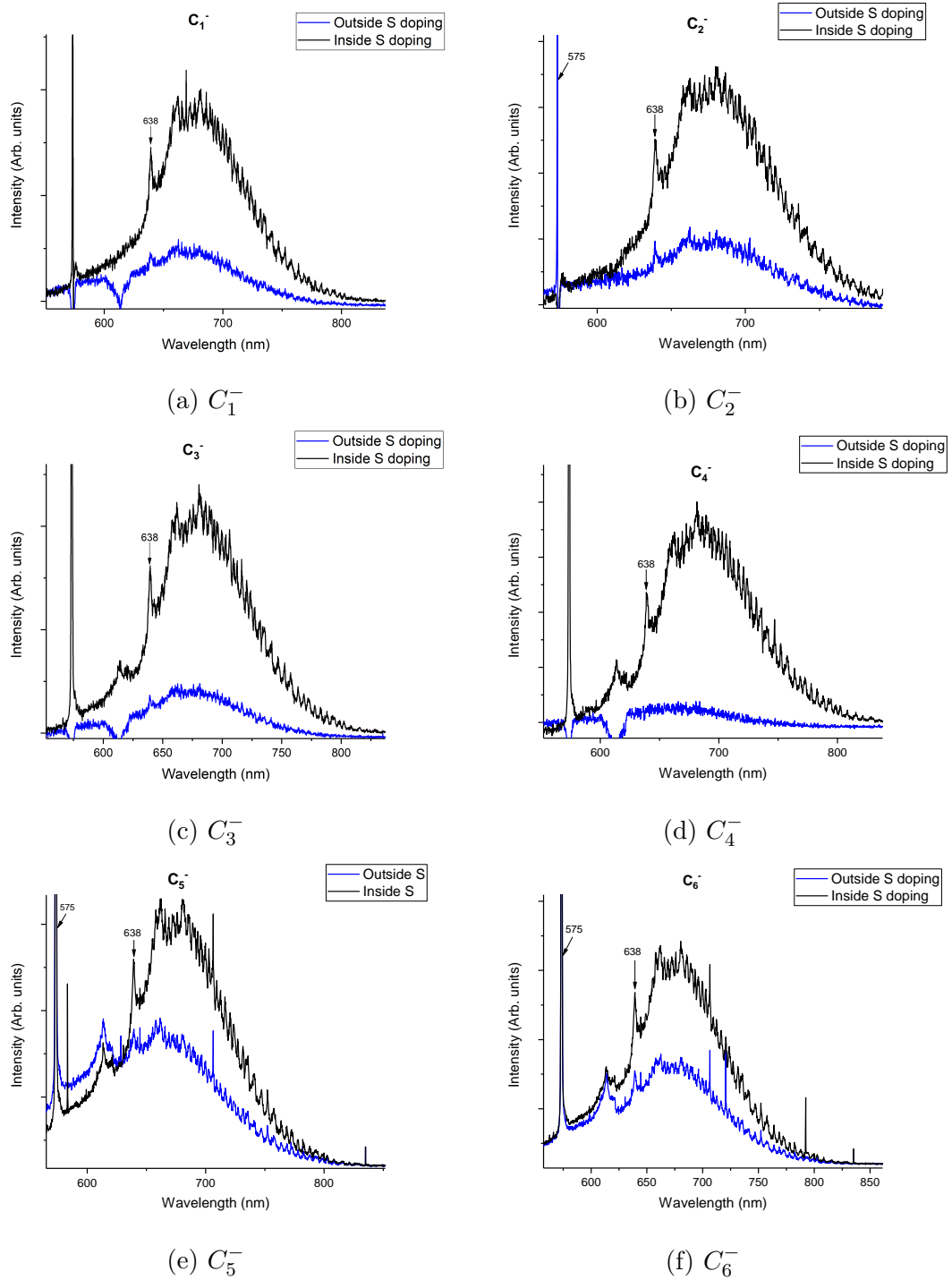
(a) C_1^-

(b) C_2^-

(c) C_3^-

(d) C_4^-

(e) C_5^-

(f) C_6^-

Figure 5.6: Spectra of the C_1^- to C_4^- ion implantation regarding the dopant S after background correction. C_5^- and C_6^- could not be background corrected. The ZPL of the NV^- is present at 638 nm with a higher intensity for the S-doped diamond in all of the samples. The phonon side bands after 638 nm of NV^- centre in the doped diamond are also clear. At 575 nm the first Raman peak of the diamond shows up.
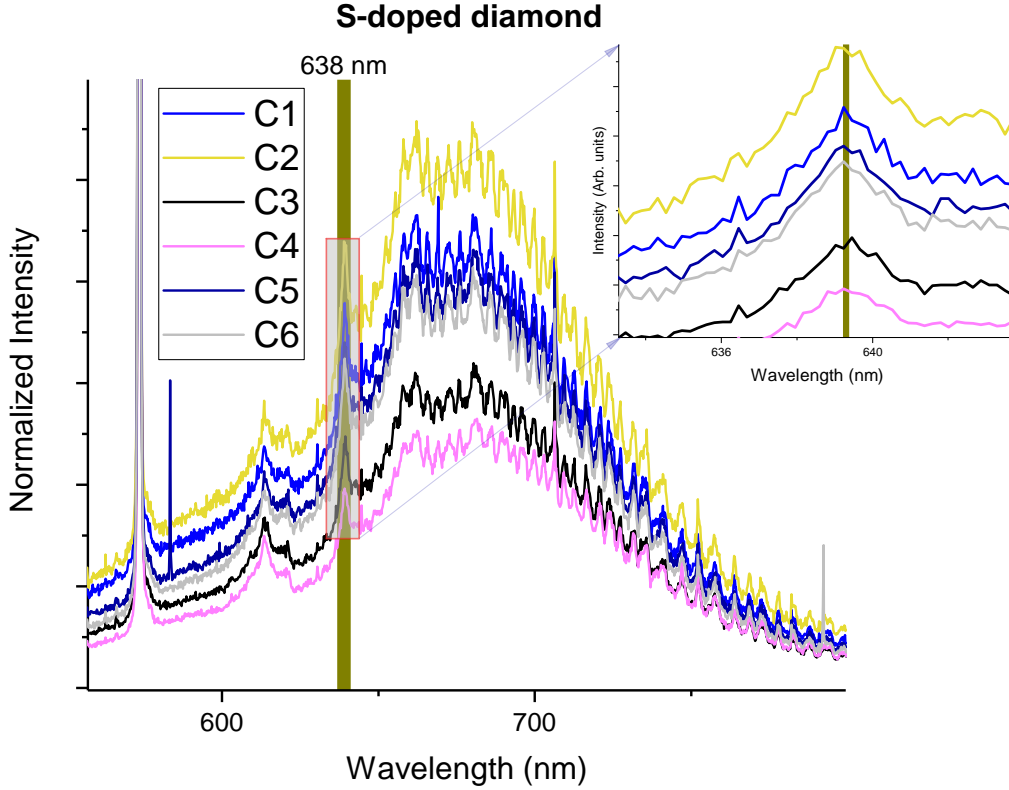
Figure 5.7: Spectra of Carbon implantations (C_1^- to C_6^-) in S-doped diamond. The normalized integrated intensity from the ZPL of NV^- to 800 nm follows a pattern depending on which carbon ionic molecule is considered. From the inset one can see that the fluorescence for $C_2^- > C_3^- > C_4^-$ and $C_1^- > C_5^- > C_6^-$.

When considering together all of the carbon implantations C_1^- to C_6^- in the S doped diamond, as shown in figure 5.7, a trend in the intensities can be identified: $C_2^- > C_3^- > C_4^-$ and $C_1^- > C_5^- > C_6^-$. The lower the number of the carbon molecule/ single ion, the higher the intensity of the NV^- ZPL. Nevertheless $C_1^- > C_2^-$ is not fulfilled maybe because possible problems in the measurements like aleatory errors or miscalibration of the equipment. A similar trend is found when analyzing the ratios inside/outside implantations (see figure 5.9).

5.2.2 NV^0 and NV^- centers in Boron doping

From the analysis of the spectra in the regions of interest, lower fluorescence intensities regarding to NV^- centers are found in the B-doped diamond (■) if compared with the outside undoped areas (see figure 5.8 (a),(d),(e) and (f); figures 5.8b and 5.8c do not follow this trend probably because inadequate background measurements). This is explained because no Coulomb repulsion between V^0 during annealing occurred in the B doped diamond that prevents vacancies forming aggregates or divacancies therefore other colour centres can be created such as

interstitial nitrogen (N_s) divacancies (V_2), N_2V, N_2 and NVH [52] rather than NV centers.

Conversely in the regions where B is absent (■), the vacancies are not kept neutral [3] thus a certain Coulomb repulsion can be expected that allows a higher yield of NV^- centers: higher intensity of the ZPL of the NV^- at 638 nm for the implantation of C_1^-, C_4^-, C_5^- and C_6^- in the figure 5.8.

When comparing the results for S and B doped diamond the previous findings are found to be opposite, which is expected due to the different behaviour of the acceptors and donors as discussed above.

5.2.3 Creation yield of NV centers

The number of NV^- centers in confocal spots of the pictures could not be determined just by counting them because of possible overlapping of fluorescence of NV's located at different but close depths, something also noted in [32]. Additionally, the high density of NV centres found along the surface of the relevant areas of the diamond prevented the possibility to find an isolated NV center whose fluorescence can be used to determine the yield.

Sulfur

In table 5.1 a ratio of the fluorescence of S-doped diamond is shown with respect to undoped regions when analysing the confocal images. The same information is calculated when comparing the area under the curve of the spectra. The mean calculated ratio when both methods are used is 2.31 ± 0.38. No mayor differences are found when the carbon molecules increase their number. Nevertheless in accordance with fig. 5.7 and fig. 5.9, a lower carbon species leads to a higher yield and it decreases with the increase of molecule number. However this contribution is small if compared with the increment of the NV centres yield due to the presence of sulfur as dopant. The literature value was found in [3] to be of 75% of yield for sulfur.

Boron

The rations between B-doped diamond and outside are presented in table 5.2, table 5.3 for six species of C. The mean value is 1.01 ± 0.22. From fig. 5.9, a lower carbon species leads to a higher yield and it decreases with the increase of molecule number.

(a) C_1^-

(b) C_2^-

(c) C_3^-

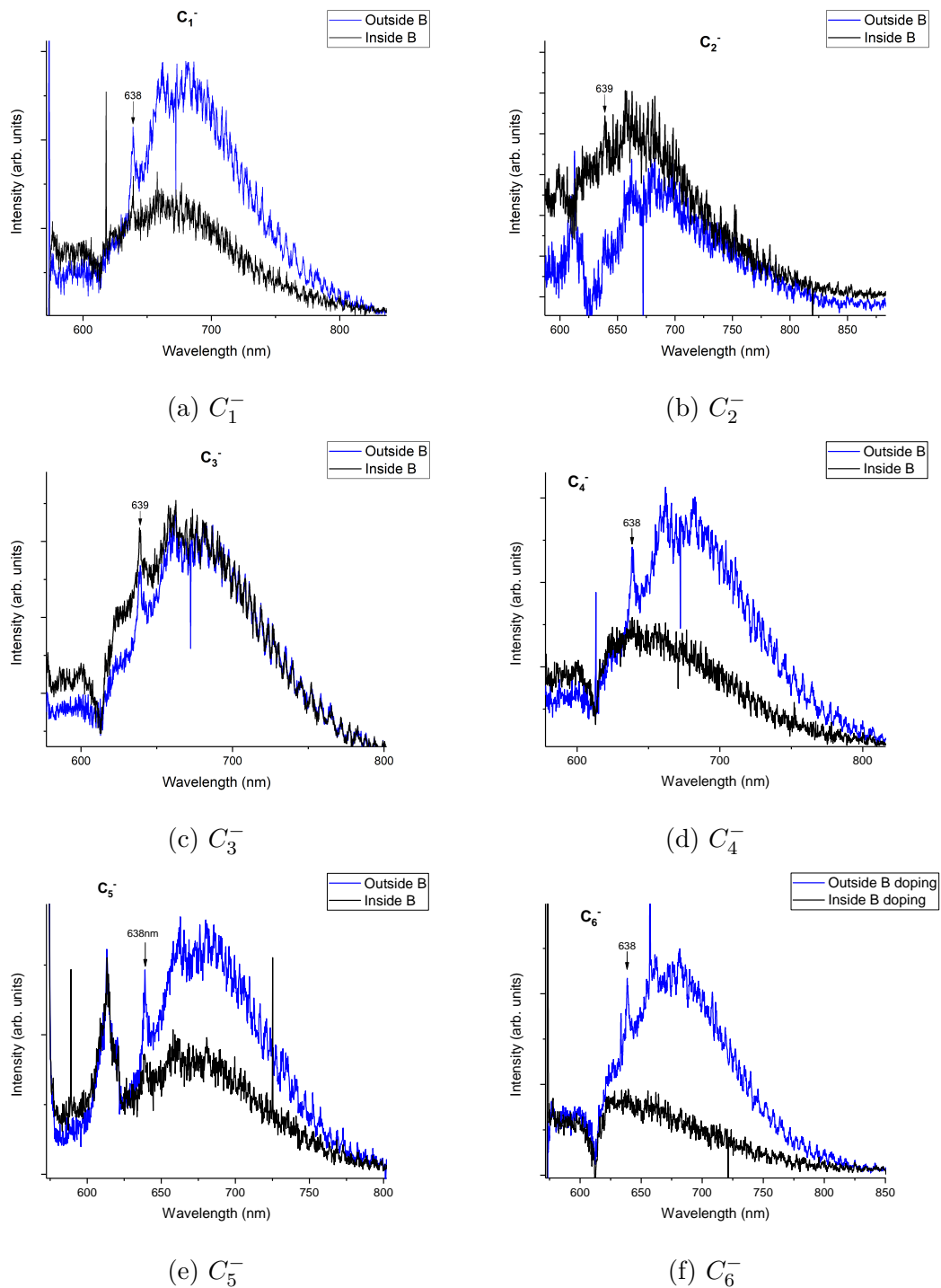(d) C_4^-

(e) C_5^-

(f) C_6^-

Figure 5.8: Spectra of the C_1^- to C_6^- ion implantation regarding the dopant B. A background correction was made using measurements from the near regions. Due to imperfections on the diamond surface for regions C_3^- and C_2^-, the spectra look different as the other ones. Note the intensity of ZPL of NV^- outside the B-doped diamond is higher as inside in most of the cases.
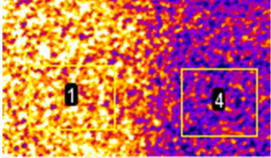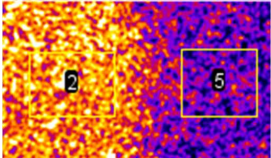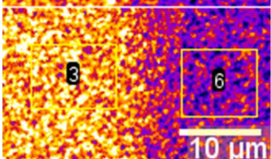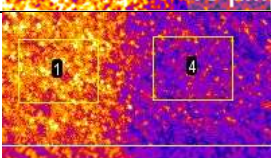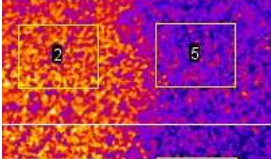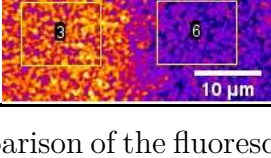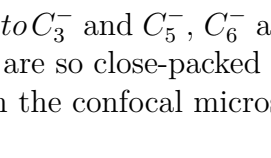
C species in Sulfur dopant	Picture		Mean fluorescence (kcounts/s) (without background correction)		Ratio
	S doping	Outside	Sulfur doping	Outside	
C_1^-			178.95	68.72	2.6
C_2^-			164.68	55.54	2.9
C_3^-			174.11	71.23	2.4
C_5^-			120.12	56.40	2.1
C_6^-			100.04	46.71	2.1
C_1^-@ 80keV			101.96	39.62	2.6

Table 5.1: Comparison of the fluorescence of NV centers formed in the implantation regions from C_1^- to C_3^- and C_5^-, C_6^- and C_1^- at 80keV when sulfur is used as dopant. The NV centers are so close-packed together than it is not possible to distinguish a single one with the confocal microscope.
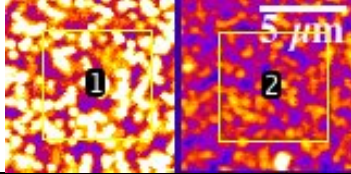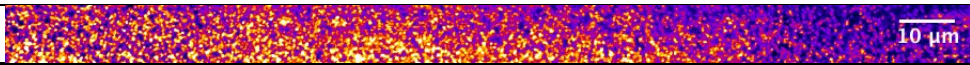
C molecule	Picture	Mean fluorescence (kcounts/s) (background corrected)		Ratio
		B doping	**Outside**	
C_2^-		1. 4751	2. 6450	0.73
Stripe showing the regions considered				
IV	**III**	**II**		**I**

Table 5.2: Comparison of the fluorescence of NV centers formed in the implantation region C_2^- when boron is used as dopant. In the last cell of the table a confocal image showing the four implantation regions is shown.

Carbon species	Ratio Ins/Outs	
	B	**S**
C_1^-	1.0	2.1
C_2^-	1.4	2.0
C_3^-	1.2	2.5
C_4^-	1.0	2.9
C_5^-	0.9	1.7
C_6^-	0.9	1.8

Table 5.3: Ratio of the integrated luminescence spectrum from ZPL at $638(5)\,\text{nm}$ to $800(5)\,\text{nm}$ for regions inside and outside the implantation of B and S.

Figure 5.9: Ratios from table 5.3 as a function of C_x^-. Both linear fits have a negative slope, which means the ratio decreases with the increase in molecule number.

Chapter 6

Summary and Outlook
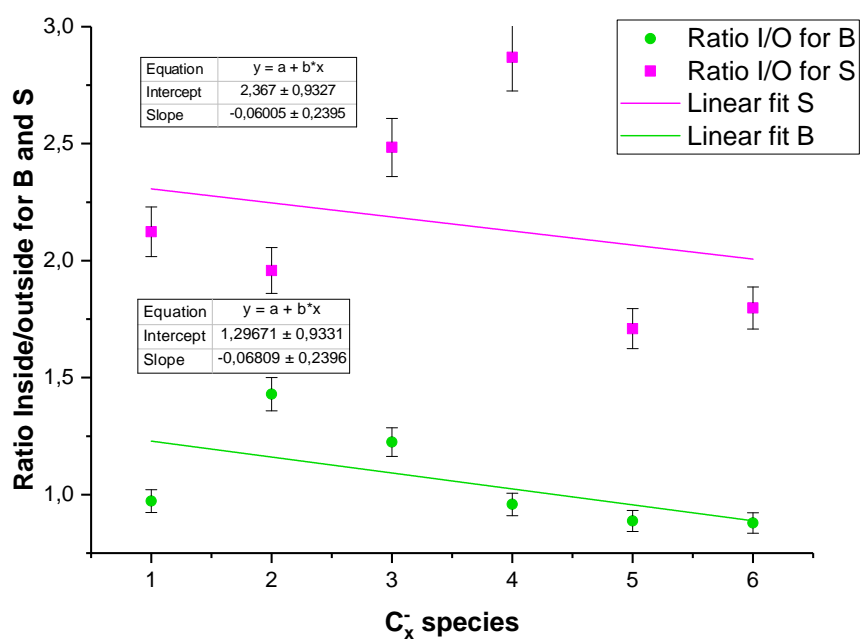
The neutrally charged vacancies were studied for S and B. It was found that the ZPL of GR1 is higher in intensity (1.37 times higher for C6 implantation) for the B-doped diamond as compared with the regions outside. In fact, the acceptor B takes the possible charges of the vacancies and stabilizes them into neutral state. These findings were inverted when S is used as dopant. In this case, the region with a higher number of neutrally charged vacancies was found outside the S-doped diamond. In fact, the fluorescence regarding V^0 was about 2,71 times higher outside the S-doped diamond for the implantation of C_6^-. Consequently in the S-doped region there exists negatively charged vacancies which repel each other according to Coulomb's law. Such repulsion prevents the formation of di-vacancies and vacancies conglomerates after annealing. Therefore, this mechanism contributes to increase the yield of NV centers by hinging the creation of undesired centres like V_2 [52]. A more quantitative analysis was not possible, since at this point NV centers were already profusely found (probably activated due to the use of the plasma chamber [48], or due to the intrinsic N concentration present in the bare diamond even though the sample was not annealed for the second time.

Regarding the NV^0 and NV^- centers creation, a higher intensity of the ZPL of NV^- centers is found in the S doped diamond as outside it. This is explained because the negative charge state requires an electron from a donor in the diamond lattice, as pointed out by [24], therefore the unpaired electron in the donor S may charge the vacancy site. In addition, the NV centre's yield is favoured by the Coulomb repulsion of the V^- vacancies. Neither the ZPL nor the phonon side bands of the NV^0 appeared in the measurements. Nevertheless the important finding here is the high yield of NV^- centres driven by the presence of sulfur as dopant [3].

For B doping the situation is opposite as for S: lower fluorescence intensities regarding NV^- centers are found in the B-doped diamond as compared with the outside undoped areas. This is explained because no Coulomb repulsion between V^0 during annealing occurred in the B doped diamond that prevents vacancies forming aggregates or divacancies therefore other colour centres can be created such as interstitial nitrogen (N_s) divacancies (V_2), N_2V, N_2 and NVH [52] rather than NV centers. Conversely in the regions where B is absent the vacancies are

not kept neutral [3] thus a certain Coulomb repulsion can be expected that allows a higher intensity of the ZPL of the NV^- for the implantation of C_1^-, C_4^-, C_5^- and C_6^-.

The creation yield of NV^- centers could not be determined because the high density of NV's along the sample prevented to identify single NV centers for comparison with the total fluorescence of a given area. Nevertheless, the mean ratio of the fluorescence of S-doped diamond with respect to the undoped regions is 2.31 ± 0.38. No mayor differences are found when C_x^- increase their number. However a lower carbon species leads to a higher yield and it decreases with the increase of molecule number. This contribution is small if compared with the high increment of the NV centres yield due to the presence of sulfur (75% in [3]). The regions concerning B-doped diamond for the implantation of C_2^- present a ratio B-doping/outside of 0.73 which means the intensity is higher in the region where B is not present. In general it is found that a higher yield of NV centers occurs when the boron is not present in the implantation.

The mean value of the ratios between B-doped diamond and outside is 1.01 ± 0.22. In general it is found that a higher yield of NV centers occurs when the boron is not present in the implantation, but since the big standard deviation this statement is not conclusive. A trend can also be identified: lower carbon species lead to a higher yield and it decreases with the increase of molecule number.

Bibliography

[1]   J.W. Hershey. *The Book Of Diamonds: Their Curious Lore, Properties, Tests And Synthetic Manufacture 1940*. Kessinger Publishing, 2004. ISBN: 9781417977154. URL: https://books.google.de/books?id=35eij1e1al8C.

[2]   D. Rabello. *Os diamantes do Brasil: na regência de Dom João, 1792-1816: um estudo de dependência externa*. Coleção Universidade aberta. Editora Arte & Ciência: UNIP, 2018. ISBN: 8586127094 9788586127090.

[3]   T. Lühmann et al. "Screening and engineering of colour centres in diamond". In: *J. Phys. D: Appl. Phys.51 483002* (2018), pp. 891–921. DOI: https://doi.org/10.1088/1361-6463/aadfab.

[4]   A. Ishaq and M. Malik. *Ion beam applications*. IntechOpen, 2018. ISBN: 9781789234145 178923414X.

[5]   L. Childress and R. Hanson. "Diamond NV centers for quantum computing and quantum networks". In: *MRS Bulletin* 38.2 (2013), 134–138. DOI: 10.1557/mrs.2013.20.

[6]   S. Pezzagna and J. Meijer. "High-Resolution Ion Implantation from keV to MeV". In: 2012.

[7]   S. Karaveli et al. "Modulation of nitrogen vacancy charge state and fluorescence in nanodiamonds using electrochemical potential". In: *Proceedings of the National Academy of Sciences* (2016). DOI: 10.1073/pnas.1504451113. eprint: https://www.pnas.org/content/early/2016/03/23/1504451113.full.pdf.

[8]   N Aslam et al. "Photo-induced ionization dynamics of the nitrogen vacancy defect in diamond investigated by single-shot charge state detection". In: *New Journal of Physics* 15.1 (2013), p. 013064. DOI: 10.1088/1367-2630/15/1/013064.

[9]   J. Barzola-Quiquia et al. "Unconventional Magnetization below 25K in Nitrogen doped Diamond provides hints for the existence of Superconductivity and Superparamagnetism". In: *Scientific Reports* 9 (June 2019), pp. 2045–2322. DOI: https://doi.org/10.1038/s41598-019-45004-6.

[10]   H. Ibach and H. Lüth. *Solid-State Physics*. Fourth Edition. Advanced texts in Physics. Springer, 2009. ISBN: 9783409380303.

[11] C. Kittel. *Introduction to Solid State Physics.* Eighth Edition. John Wiley & Sons, Inc, 2005. ISBN: 047141526-X.

[12] N. Ashcroft and D. Mermin. *Solid State Physics.* Harcourt College Publishers, 1976. ISBN: 0030839939.

[13] D. Roundy. *Periodic Systems Metals and Insulators.* Last Visited 16/01/2020. 2019. URL: http://physics.oregonstate.edu/~roundyd/COURSES/ph427/metal-insulator-worksheet.html.

[14] J. Sólyom. *Fundamentals of the Physics of Solids. Electronic Properties.* Vol. 2. Springer, 2003. ISBN: 9783540853152.

[15] W. Saslow and Bergstresser T. "Band Structure and optical properties of diamond". In: *Physical Review Letters* 16.9 (1966), pp. 354–356.

[16] B. K. Ridley. *Quantum Processes in Semiconductors.* Fifth Edition. OXFORD, 2013. ISBN: 9780199677214.

[17] G Calzaferri and R Rytz. "The Band Structure of Diamond". In: *J. Phys. Chem.* 100 (1996), pp. 11122–11123.

[18] M. Nazaré and A. Neves. *Properties, Growth and Applications of Diamond.* INSPEC, 2001. ISBN: 0852967853.

[19] A. Zaitsev. *Optical Properties of Diamond. A Data Handbook.* Springer, 2000. ISBN: 9783540665823.

[20] F. Jelezko and J. Wrachtrup. "Single defect centres in diamond: A review". In: *phys. stat. sol.* 203.13 (2006), pp. 3207–3225. DOI: 10.1002/pssa.200671403.

[21] C Breeding and J Shigley. "The "Type" Classification System of Diamonds and Its Importance in Gemology". In: *Gems & Gemology* 45.2 (Summer 2009), pp. 96–101.

[22] Element Six^{TM}. *The element six CVD diamond Handbook.* Last Visited 20/01/2020. URL: https://e6-prd-cdn-01.azureedge.net/mediacontainer/medialibraries/element6/documents/brochures/element_six_cvd_diamond_handbook.pdf?ext=.pdf.

[23] B. Fortman and S. Takahashi. "Understanding the Linewidth of the ESR Spectrum Detected by a Single NV Center in Diamond". In: *Journal of physical chemistry* 123 (2019), pp. 6350–6355. DOI: 10.1021/acs.jpca.9b02445.

[24] N. Manson et al. "$NV^- - N^+$ pair centre in 1b diamond". In: *New J. Phys.* 20.113037 (2018). DOI: https://doi.org/10.1088/1367-2630/aaec58.

[25] R. Hanson et al. "Coherent Dynamics of a Single Spin Interacting with an Adjustable Spin Bath". In: *Science* 320.5874 (2008), pp. 352–355. DOI: 10.1126/science.1155400. URL: https://science.sciencemag.org/content/320/5874/352.

[26] T. Abtew, Y. Sun, and B. Shih. "Dynamic Jahn-Teller Effect in the NV^- Center in Diamond". In: *Physical review letters* 107.123 (2011), pp. 146403–146405. DOI: 10.1103/PhysRevLett.107.146403.

[27] M. S. Dresselhaus and R. Kalish. *Ion Implantation in Diamond, Graphite and Related Materials.* Springer, 1992. ISBN: 9783642771712.

[28] J. Ziegler, J. Biersack, and M. Ziegler. *SRIM. The Stopping and Range of Ions in Matter.* Seventh Edition. SRIM Co., 2008. ISBN: 9780965420716.

[29] R. Wunderlich. *Methodische Entwicklungen zur quantitativen ortsaufgelösten Ionenstrahlanalytik von lateral stark inhomogenen Meteoritenproben.* Universität Leipzig. Fakultät für Physik und Geowissenschaften. Masterarbeit. 2012.

[30] J. Ziegler. *Stopping and Range of Ions in Matter SRIM Software.* Version SRIM-2008,04. 2008. URL: http://www.srim.org/index.htm#HOMETOP.

[31] T. Alford, C. Feldman, and J. Mayer. *Fundamentals of Nanoscale Film Analysis.* Springer, Boston, MA, 2007. ISBN: 9780387292618.

[32] S. Trofimov et al. "Spatially controlled fabrication of single NV centers in IIa HPHT diamond". In: *Optical Materials Express* 10 (Jan. 2020), p. 198. DOI: 10.1364/OME.10.000198.

[33] S Pezzagna et al. "Creation efficiency of nitrogen-vacancy centres in diamond". In: *New Journal of Physics* 12.6 (2010), p. 065017. DOI: 10.1088/1367-2630/12/6/065017.

[34] National Electrostatics Corp. *Source of Negative Ions by Cesium Sputtering - SNICS II.* Last Visited 04/02/2020. URL: https://www.pelletron.com/wp-content/uploads/2017/02/SNICS-v2.pdf.

[35] M Rani Jana. *Dynamics and kinetics of ion impact dissociation of molecules.* University of Calcutta. Dept. of Physics. PhD Thesis. 2012.

[36] J. Küpper. *Änderung des Ladungszustandes von NV-Zentren durch p-i-p Dioden in Diamant.* Universität Leipzig. Fakultät für Physik und Geowissenschaften. Masterarbeit. 2017.

[37] R. Staake. *Magnetometrie nicht klassischer Leitungsmechanismen in amorphen Halbleitern mit Hilfe einzelner NV^- Zentren.* Universität Leipzig. Masterarbeit. 2015.

[38] R.D. Cowan et al. "Excited states of the negative nitrogen ion: energies and lifetimes". In: *Journal of Physics B: Atomic, Molecular and Optical Physics* 30.6 (1997), pp. 1457–1466. DOI: 10.1088/0953-4075/30/6/014. URL: https://doi.org/10.1088%2F0953-4075%2F30%2F6%2F014.

[39] Diener Electronic. *Low-presure plasma.* Last Visited 31/01/2020. 2016. URL: https://www.plasma.com/es/plasmatechnik/lexikon/sistema-de-plasma/.

[40] T. Wilson. *Confocal Microscopy*. Fifth Edition. Academic Press Limited, 1990. ISBN: 0127572708.

[41] T. Wilson. "Resolution and optical sectioning in the confocal microscope". In: *Journal of Microscopy* 244.2 (2011), pp. 113–121. DOI: 10 . 1111 / j . 1365 – 2818 . 2011 . 03549 . x. eprint: https : / / onlinelibrary . wiley . com / doi / pdf / 10 . 1111 / j . 1365 – 2818 . 2011 . 03549 . x. URL: https : //onlinelibrary.wiley.com/doi/abs/10.1111/j.1365-2818.2011. 03549.x.

[42] R. H. Webb. "Confocal optical microscopy". In: *Reports on Progress in Physics* 59.3 (1996), pp. 427–471. DOI: 10 . 1088 / 0034 – 4885 / 59 / 3 / 003. URL: https://doi.org/10.1088%2F0034-4885%2F59%2F3%2F003.

[43] C. Bräutigam. *Untersuchung zur Auswirkung einer niederfrequenten Sauerstoffplasmabehandlung auf oberflächennahe NV-Zentren im Diamanten*. Universität Leipzig. Fakultät für Physik und Geowissenschaften. Bachelorarbeit. 2017.

[44] Excelitas Technologies. *High-Performance Single Photon Counting Modules. SPCM Product Series*. Last Visited 08/02/2020. URL: https://www.excelitas. com/product-category/single-photon-counting-modules.

[45] Element Six^{TM}. *Product description*. Last Visited 17/09/2019. 2019. URL: https://e6cvd.com/us/application/all/el-sc-plate-2-0x2-0x0- 5mm.html.

[46] R Löfgren et al. "The bulk conversion depth of the NV-center in diamond: computing a charged defect in a neutral slab". In: *New Journal of Physics* 21.5 (2019), p. 053037. DOI: 10.1088/1367-2630/ab1ec5.

[47] T. Lühman et al. "Coulomb-driven single defect engineering for scalable qubits and spin sensors in diamond". In: *Nature comunications* (2019). DOI: https://doi.org/10.1038/s41467-019-12556-0.

[48] C. Osterkamp et al. "Increasing the creation yield of shallow single defects in diamond by surface plasma treatment". In: *Applied Physics Letters* 103.19 (2013), pp. 146403–146405. DOI: https://doi.org/10.1063/1.4829875.

[49] A. Collins and A. Dahwich. "The production of vacancies in type Ib diamond". In: *Journal of Physics-condensed Matter - J PHYS-CONDENS MATTER* 15 (Sept. 2003), p. L591. DOI: 10.1088/0953-8984/15/37/L06.

[50] J. Isoya et al. "EPR identification of the negatively charged vacancy in diamond". In: *Phys. Rev. B* 45 (3 1992), pp. 1436–1439. DOI: 10 . 1103 / PhysRevB . 45 . 1436. URL: https : / / link . aps . org / doi / 10 . 1103 / PhysRevB.45.1436.

[51] National Institutes of Health. *ImageJ Software*. Version 1.52q 13 September 2019. 2019. URL: https://imagej.nih.gov/ij/index.html.

[52] P. Deák et al. "Formation of NV centers in diamond: A theoretical study based on calculated transitions and migration of nitrogen and vacancy related defects". In: *Phys. Rev. B* 89 (7 2014), p. 075203. DOI: 10.1103/PhysRevB.89.075203. URL: https://link.aps.org/doi/10.1103/PhysRevB.89.075203.

Page intentionally left blank.

Acknowledgements

I would like to first and foremost thank Prof. Dr. Meijer for incorporating me in his division. I would especially like to thank Dr. Ralf Wunderlich for tutoring this thesis, reading the drafts and correcting my numerous naive assumptions. Without his help in those aspects, I could not have progressed successfully.

I am indebted to Tobias Luhman for his patience in explaining me important concepts and for preparing the set up of the confocal microscope for me to use. I wish also to thank all the people whose assistance was a milestone in the completion of this work: Tobias Herzig and Dr. Michael Kieschnick for their support in the implantations. Clemens for the interesting speeches and support in the use of the Confocal microscope and the people that were there to help me: Sascha, Florian, Robert and all of the members of the Division of Advanced Quantum Systems of the Physics Faculty of the Leipzig University.

I wish finally to acknowledge the support and great love of my mother Julia Pazmiño who was always supporting me from the other side of the Atlantic Ocean and who I have not seen since I started the Bachelor.

Page intentionally left blank.

Declaration of Originality

I hereby confirm, that I have written this thesis independently and without illicit help of others. No other sources, but those given in the bibliography, were used. No other persons work has been used in this thesis without due acknowledgement. All references and verbatim extracts have been quoted, and all sources of information, including graphs and diagrams, have been specifically acknowledged.

_____

Efrain Insuasti Pazmiño
Leipzig, March 2020.